

The hot circumgalactic medium in the eROSITA All-Sky Survey

I. X-ray surface brightness profiles

Yi Zhang^{1,*}, Johan Comparat¹, Gabriele Ponti^{2,1}, Andrea Merloni¹, Kirpal Nandra¹, Frank Haberl¹, Nicola Locatelli², Xiaoyuan Zhang¹, Jeremy Sanders¹, Xueying Zheng¹, Ang Liu¹, Paola Popesso³, Teng Liu^{4,5}, Nhut Truong^{6,7}, Annalisa Pillepich⁸, Peter Predehl¹, Mara Salvato¹, Soumya Shreeram¹, Michael C. H. Yeung¹, and Qingling Ni¹

¹ Max-Planck-Institut für extraterrestrische Physik (MPE), Gießenbachstraße 1, D-85748 Garching bei München, Germany

² INAF-Osservatorio Astronomico di Brera, Via E. Bianchi 46, I-23807 Merate (LC), Italy

³ European Southern Observatory, Karl Schwarzschildstrasse 2, D-85748 Garching bei München, Germany

⁴ Department of Astronomy, University of Science and Technology of China, Hefei 230026, China

⁵ School of Astronomy and Space Science, University of Science and Technology of China, Hefei 230026, China

⁶ NASA Goddard Space Flight Center, Greenbelt, MD 20771, USA

⁷ Center for Space Sciences and Technology, University of Maryland, 1000 Hilltop Circle, Baltimore, MD 21250, USA

⁸ Max-Planck-Institut für Astronomie, Königstuhl 17, 69117 Heidelberg, Germany

August 20, 2024

ABSTRACT

Context. The circumgalactic medium (CGM) provides the material needed for galaxy formation and influences galaxy evolution. The hot ($T > 10^6$ K) CGM is poorly detected around galaxies with stellar masses (M_*) lower than $3 \times 10^{11} M_\odot$ due to the low surface brightness.

Aims. We aim to detect the X-ray emission from the hot CGM around Milky Way-mass (MW-mass, $\log(M_*/M_\odot) = 10.5 - 11.0$) and M31-mass ($\log(M_*/M_\odot) = 11.0 - 11.25$) galaxies, in addition to measuring the X-ray surface brightness profile of the hot CGM.

Methods. We applied a stacking technique to gain enough statistics to detect the hot CGM. We used the X-ray data from the first four SRG/eROSITA All-Sky Surveys (eRASS:4). We discussed how the satellite galaxies could bias the stacking and the method we used to carefully build the central galaxy samples. Based on the SDSS spectroscopic survey and halo-based group finder algorithm, we selected central galaxies with spectroscopic redshifts of $z_{\text{spec}} < 0.2$ and stellar masses of $10.0 < \log(M_*/M_\odot) < 11.5$ (85,222 galaxies) – or halo masses of $11.5 < \log(M_{200\text{m}}/M_\odot) < 14.0$ (125,512 galaxies). By stacking the X-ray emission around galaxies, we obtained the mean X-ray surface brightness profiles. We masked the detected X-ray point sources and carefully modeled the X-ray emission from the unresolved active galactic nuclei (AGN) and X-ray binaries (XRB) to obtain the X-ray emission from the hot CGM.

Results. We measured the X-ray surface brightness profiles for central galaxies of $\log(M_*/M_\odot) > 10.0$ or $\log(M_{200\text{m}}/M_\odot) > 11.5$. We detected the X-ray emission around MW-mass and more massive central galaxies extending up to the virial radius (R_{vir}). The signal-to-noise ratio (S/N) of the extended emission around MW-mass (M31-mass) galaxy is about 3.1σ (4.7σ) within R_{vir} . We used a β model to describe the X-ray surface brightness profile of the hot CGM ($S_{\text{X,CGM}}$). We obtained a central surface brightness of $\log(S_{\text{X,0}}[\text{erg s}^{-1} \text{kpc}^{-2}]) = 36.7_{-0.4}^{+1.4}$ ($37.1_{-0.4}^{+1.5}$) and $\beta = 0.43_{-0.06}^{+0.10}$ ($0.37_{-0.02}^{+0.04}$) for MW-mass (M31-mass) galaxies. For galaxies with $\log(M_{200\text{m}}/M_\odot) > 12.5$, the extended X-ray emission is detected with $S/N > 2.8\sigma$ and the $S_{\text{X,CGM}}$ can be described by a β model with $\beta \approx 0.4$ and $\log(S_{\text{X,0}}[\text{erg s}^{-1} \text{kpc}^{-2}]) > 37.2$. We estimated the baryon budget of the hot CGM and obtained a value that is lower than the prediction of Λ CDM cosmology, indicating significant gas depletion in these halos. We extrapolated the hot CGM profile measured within R_{vir} to larger radii and found that within $\approx 3R_{\text{vir}}$, the baryon budget is close to the Λ CDM cosmology prediction.

Conclusions. We measured the extended X-ray emission from representative populations of central galaxies around and above MW-mass out to R_{vir} . Our results set a firm footing for the presence of the hot CGM around such galaxies. These measurements constitute a new benchmark for galaxy evolution models and possible implementations of feedback processes therein.

Key words. X-ray, galaxies, circum-galactic medium

1. Introduction

The circumgalactic medium (CGM) is the gas reservoir of a galaxy and it is closely related to galaxy evolution processes. Understanding the properties of the CGM is essential to the study of galaxy formation and evolution, for example, the strength of feedback processes and how they modulate the star formation and gas activity (Tumlinson et al. 2017; Naab & Ostriker 2017; Truong et al. 2020, 2021; Eckert et al. 2021; Oppenheimer et al. 2021). The observed CGM has multiple phases. Its temperature

(T) ranges from $< 10^4$ K to $> 10^6$ K. The cold ($T < 10^4$ K), cool ($T = 10^4 - 10^5$ K) and warm ($T = 10^5 - 10^6$ K) phases of CGM have been well studied (Prochaska et al. 2011; Tumlinson et al. 2011; Putman et al. 2012; Werk et al. 2014, 2016; Prochaska et al. 2017). The next vital target is to attain a complete picture of the relationship between the galaxy and its hot ($T > 10^6$ K) phase of the CGM.

The hot phase of the CGM is the dominant mass component of the CGM baryon budget (Tumlinson et al. 2017). This hot CGM can be heated and shaped by the gravitational accretion shock and feedback processes, for example, active galactic

* yizhang@mpe.mpg.de

nucleus (AGN) and stellar feedback. It emits X-rays via collisionally ionized gas emission lines, recombination lines and bremsstrahlung. Pointed observations using *Chandra* or *XMM-Newton* revealed the hot gas properties of a few nearby galaxies within a distance of 50 Mpc (Strickland et al. 2004; Tüllmann et al. 2006; Wang 2010; Dai et al. 2012; Li & Wang 2013; Bogdán et al. 2013, 2015; Anderson et al. 2016; Li et al. 2016). The hot gas surveys of *Chandra* and *XMM-Newton* focus on the inner hot CGM (or the "corona") with scale heights of about 1–30 kpc (median of 5 kpc), where feedback processes dominate over gravitation. With their spatial resolution, *XMM-Newton* and especially *Chandra* resolve the stellar structures distributed in the disk of nearby galaxies. Still, the availability of galaxies with the detectable extended emission of the CGM is limited in number and extension.

For the outer hot CGM, where virialized gas dominates, to heat the gas to X-ray emitting temperature over the radiation cooling curve through gravitation, M_{halo} needs to be high enough (typically $>10^{12.7} M_{\odot}$). This corresponds to massive galaxies with about $M_* > 10^{11} M_{\odot}$ (Kereš et al. 2009b,a; van de Voort et al. 2016; Li et al. 2016; Liu et al. 2022). For these reasons, although the hot gas in galaxy groups and clusters has been detected and studied well (Pratt et al. 2019; Walker et al. 2019), very few detections of the outer hot CGM (out to 70 kpc) from galaxies have been reported (Dai et al. 2012; Bogdán et al. 2013, 2015; Anderson et al. 2016; Li et al. 2016; Das et al. 2020).

To chart the CGM outer emission beyond the Local Universe, we use stacking techniques to detect its faint emission, provided large enough volumes are surveyed. By stacking about 250,000 "locally brightest galaxies" selected from the Sloan Digital Sky Survey (SDSS) and using data from ROSAT All-Sky Survey, Anderson et al. (2015) detected hot gas emission around $M_* > 10^{10.8} M_{\odot}$ galaxies. In addition, X-ray observations and studies of the CGM with the thermal Sunyaev–Zeldovich (tSZ) effect have progressed in recent years; for example, with the Atacama Cosmology Telescope (ACT, Aiola et al. 2020). The thermal energy density profile of the CGM is measured around $M_* > 10^{10.6} M_{\odot}$ galaxies by cross-correlating and stacking the WISE and SuperCOSMOS photometric redshift galaxy sample with ACT and Planck (Bilicki et al. 2016; Das et al. 2023).

X-ray stacking experiments are now dramatically progressing thanks to the extended ROentgen survey with an Imaging Telescope Array (eROSITA) on board the Spektrum-Roentgen-Gamma (SRG) orbital observatory. Launched in 2019, eROSITA is a sensitive X-ray telescope performing all-sky surveys with a wide-field focusing telescope (Merloni et al. 2012; Predehl et al. 2021; Sunyaev et al. 2021; Merloni et al. 2024). The sensitivity of eROSITA is maximal in the soft energy band, namely below 2.3 keV, which makes it suitable for studying the million-degrees hot CGM emission. Recently, with eROSITA and its PV/eFEDS observations covering 140 deg², Comparat et al. (2022) stacked ~16,000 central galaxies selected from the Galaxy And Mass Assembly (GAMA) spectroscopic galaxy survey; later, Chadayammuri et al. (2022) stacked ~1,600 massive galaxies selected from SDSS in the same eFEDS field. Both works detected and measured weak X-ray emission from the outer CGM of those galaxies by stacking star-forming and quiescent galaxies separately. The difference in the sample selection has led to different interpretations of the results.

At the time of writing, four of the planned eight all-sky surveys (eROSITA all-sky survey, eRASS:4), each lasting six months, have been completed. The X-ray data currently available for CGM stacking are about 40 times larger than what was available for the eFEDS region (100 times more area covered with

about 40% the exposure time). In this work and the accompanying papers, we stack the eRASS:4 X-ray data and a set of galaxy samples with high statistical completeness. We study the X-ray surface brightness¹ profile of the hot CGM. In the companion papers based on the same samples, we investigate (i) the scaling relations between X-ray luminosity, stellar mass, and halo mass (Zhang et al. 2024); (ii) the trends as a function of specific star formation rate (Zhang et al., in prep); and (iii) the possible azimuthal dependence of the hot CGM emission (Zhang et al., in prep).

We organize this paper as follows. We introduce the eROSITA X-ray data reduction and stacking method in Sect. 2. We define the galaxy samples in Sect. 3. We describe the models (AGN, XRB) and mock galaxy catalogs in Sect. 4. We present the mean X-ray surface brightness profiles of the complete galaxy population in Sect. 5. We show the X-ray surface brightness profiles of central galaxies and their hot CGM in Sect. 6. We estimate the baryon budget for the central galaxies in Sect. 7. Throughout the paper, we use Planck Collaboration et al. (2020) cosmological parameters: $H_0 = 67.74 \text{ km s}^{-1} \text{ Mpc}^{-1}$ and $\Omega_m = 0.3089$. All instances of log in this work are in base 10.

2. X-ray data reduction and stacking method

In this section we describe the reduction of the X-ray data (Sect. 2.1), stacking method (Sect. 2.2), and calculation of the uncertainties (Sect. 2.3), along with the PSF and β models (Sect. 2.4).

2.1. X-ray data reduction

We used the eRASS:4 data in the western Galactic hemisphere ($179.9442^\circ < l \leq 359.9442^\circ$). For the analysis, we used the eROSITA Science Analysis Software System (eSASS; Brunner et al. 2022) data products (version 020) (Merloni et al. 2024). We staged the data in 2439 overlapping sky tiles, each covering $3.6^\circ \times 3.6^\circ$. For each sky tile, we had energy-calibrated event files, vignetting-corrected mean exposure map in three bands (0.3–0.6 keV, 0.6–1.0 keV, 1.0–2.0 keV), and a catalog of detected sources in the 0.2–2.3 keV band down to a low detection likelihood of $\text{DET_LIKE_0} > 5$. We used the default flag and keep all events with valid patterns. eROSITA has seven telescope modules (TMs); two TMs suffer from light leaks (TM5 and 7; Predehl et al. 2021) and have a higher background. We used all seven telescope modules (TMs) in our analysis. We have verified that the inclusion of the two light-leak cameras (TM5 and 7) does not affect our results². The vignetted exposure time of eRASS:4, in the 0.5–2 keV band, ranges from 300s to 10,000s, with a median value of 550 s.

To account for the absorption from the Galactic neutral hydrogen, we masked the sky area where $N_{\text{H}} > 10^{21} \text{ cm}^{-2}$ as traced by the integrated HI4PI column density map (HI4PI Collaboration et al. 2016). The dust extinction and reddening in the Milky Way could cause inaccuracies in galaxy parameters. Using the thermal dust emission model from Planck observation (Planck Collaboration et al. 2014) as a proxy, we kept only the sky regions with $E(B - V) < 0.1$.

¹ In this work and companion papers, we define the surface brightness as the luminosity of the source per square kiloparsec, see Eq. 2.

² We compared the stacking results when including or excluding the TM5 and TM7; without these two TMs, the background is lower while the statistics are worse. Our stacking results are independent of their inclusion.

The source detection pipeline of eROSITA may fail around bright sources (for example, Sco X-1 and the Virgo cluster) (Merloni et al. 2024). We masked these overdense source-detection regions where potentially spurious sources are clustered (see the masking procedure in Merloni et al. (2024)). After applying the mask, about 11,000 deg² covered by X-ray observations (A_X) remained.

2.2. Stacking method

We adopted the stacking method of Comparat et al. (2022). For each galaxy in the sample, we created an event cube by retrieving events within 3 Mpc around the galaxy (CUBE_{event}). Each event cube contains the following information for each event in the cube: the position (RA, DEC), the angular separation and physical distance³ (R_{rad} and R_{kpc}) to the associated galaxy, the exposure time, t_{exp} , the observed energy, E_{obs} , the corresponding rest frame energy, $E_{\text{rest}} = E_{\text{obs}} \times (1 + z)$, and the effective area, A_{eff} , of the telescope at the observed energy. In the case of masking sources detected by eRASS:4, we took the masking radius of each source conservatively as $1.4 \times R_{\text{src}}$ to avoid residual emission, where R_{src} is the source radius derived from srctool (see Appendix A of Comparat et al. 2023). A mask flag is assigned to an event if it falls in these masked regions.

Stacking a galaxy sample consists of merging the event cubes for all galaxies in the sample and extracting a summary statistic. Each event is assigned a weight:

$$W_e = E_{\text{obs}} \frac{1}{t_{\text{exp}}} \frac{f_{\text{nh}} A_{\text{corr}} 4\pi D_L^2}{A_{\text{eff}}} [\text{erg s}^{-1} \text{Mpc}^2 \text{cm}^{-2}], \quad (1)$$

where D_L is the luminosity distance to the galaxy. Also, f_{nh} is a function that corrects the effects of absorption on the soft X-ray photons as a function of the E_{obs} and N_{H} (taken from HI4PI Collaboration et al. (2016)). We obtain f_{nh} using the TBABS absorption model (Wilms et al. 2000). A_{corr} is an area correction factor that accounts for the area loss due to masking X-ray sources.

The X-ray surface brightness profile around galaxies ($S_{X,\text{gal}}$) is calculated by selecting the events located in radial bins ($r_0 < R_{\text{kpc}} < r_1$) and summing them up as:

$$S_{X,\text{gal}} = \sum_{r_0}^{r_1} \frac{W_e}{A_{\text{shell}} N_g} [\text{erg s}^{-1} \text{kpc}^{-2}], \quad (2)$$

where A_{shell} is the area of each radial bin and N_g is the number of galaxies stacked⁴.

The background surface brightness ($S_{X,\text{bg}}$) is taken as the minimum value of $S_{X,\text{gal}}$ ($S_{X,\text{min}}$) beyond R_{500c} ⁵. We detail the background estimation procedure validation in Appendix. A. Throughout this work, we use the energy bin 0.5 – 2 keV (in rest frame) to calculate the X-ray surface brightness.

2.3. Uncertainty calculation

The uncertainty on $S_{X,\text{gal}}$ contains two components: the Poisson error from the data and the uncertainties from the stacking pro-

³ The physical (proper) distance between events and galaxies are derived according to the redshift of the galaxy and angular separation.

⁴ The radial bin boundaries used are (0, 10, 30, 50, 75, 100, 150, 200, 250, 300, 350, 400, 500, 600, 700, 800, 900, 1000, 1100, 1200, 1300, 1400, 1600, 1800, 2000, 2200, 2400, 2600, 2800, 3000) kpc.

⁵ R_{500c} is the radius where the density is 500 times the background universe critical density.

cess. We estimated the Poisson error of the X-ray surface brightness profile by $1/\sqrt{n_{\text{total}}}$, where n_{total} is the total event numbers in the corresponding radial bin.

The uncertainties from the stacking process were computed using the Jackknife re-sampling method (Andrae 2010; McIntosh 2016) to assess the X-ray property variation of the stacked galaxy population. For a galaxy sample containing N_{gal} galaxies, we randomly selected $0.9N_{\text{gal}}$ galaxies from the sample, then stacked the $0.9N_{\text{gal}}$ galaxies and obtain the mean $S_{X,\text{gal}}$ of them. We repeated the above procedure 50 times and retrieved the standard deviation of the 50 mean $S_{X,\text{gal}}$ as the uncertainty from the stacking process.

For reference, the uncertainties in our study are dominated by the standard deviation of the mean $S_{X,\text{gal}}$, which reflects the intrinsic scatter in the X-ray surface brightness of the stacked galaxy population. It is therefore possible to obtain smaller overall uncertainties of $S_{X,\text{gal}}$ using a masked sample despite its lower photon statistics, since masking significantly decreases the stacking uncertainties coming from point sources.

2.4. Point spread function and β models

We used the eROSITA point spread function (PSF) model to assess the extended nature of the observed surface brightness profile. We also used it to model the surface brightness profiles of point sources. We used the eROSITA PSF model from Sanders et al. (in prep; also, Merloni et al. (2024)). The PSF is expressed in angular units. We use the redshifts of the galaxies to convert it to a physical scale (kpc). For each galaxy sample, we convolve the PSF profile (in kpc) with the redshift distribution⁶. The extent of the X-ray emission was assessed by scaling the mean PSF profile to the central surface brightness observed to obtain a maximal PSF-like surface brightness profile. If excess emission (above the maximal PSF-like profile) is measured at large radii, then the X-ray emission must come from a source with an extension beyond that of the PSF, for example: the hot CGM.

The β model (Cavaliere & Fusco-Femiano 1976) is used to describe the X-ray profiles of the hot CGM:

$$S_{X,\beta} = S_{X,0} \left[1 + \left(\frac{r}{r_c} \right)^2 \right]^{-3\beta + \frac{1}{2}} [\text{erg s}^{-1} \text{kpc}^{-2}], \quad (3)$$

where $S_{X,0}$ is the X-ray surface brightness at the galaxy center, r is the distance from the center, and r_c is the core radius. We convolved the β profile with the PSF and built the likelihood function. We fit the PSF-convolved β model to the observation using the Markov chain Monte Carlo (MCMC) method. We took the best-fit value as the median value of the possible parameters from the MCMC and the values at 16th and 84th percentiles from MCMC as the 1σ uncertainties (Hogg et al. 2010).

3. Galaxy samples selection

We built our galaxy samples based on two criteria: (i) completeness (>90%) to reduce selection effects and (ii) size, whereby the larger, the better.

⁶ This assumes that the luminosity of the point sources in the stacked galaxies does not strongly depend on the redshift. The empirical XRB luminosity scales as $(1+z)^{3.79 \pm 0.12}$ (Aird et al. 2017), and the maximum redshift of our galaxy sample is 0.2. This suggests an evolution of less than two times. Detected X-ray point sources are masked, leaving only undetected ones in the stack. This justifies this assumption.

In this section, we calculate the maximum redshift limited by the angular resolution of eROSITA and the required galaxy survey depth to build a complete galaxy sample (Sect. 3.1). Based on the two criteria above, we select the Sloan Digital Sky Survey data release 7 (SDSS DR7) spectroscopic galaxy catalog and DESI Legacy Survey data release 9 (DESI LS DR9) photometric galaxy catalog to build the galaxy samples (Sect. 3.2).

We outline the galaxy samples and their purpose in Sect. 3.3. We explain the constructions of samples in the following sections: We describe the FULL_{spec} and FULL_{phot} samples in Sect. 3.4. We discuss the connection between galaxies and their dark matter halos in Sect. 3.5 and how the presence of satellite galaxies in the sample could bias the stacking result (Sect. 3.6). To minimize such bias, we define the central galaxy samples (CEN and CEN_{halo}) based on the SDSS spectroscopic galaxy survey (Sect. 3.7) and an isolated galaxy sample based on LS DR9 photometric galaxy catalog (Appendix. D).

3.1. Considerations on the maximum redshift and galaxy survey depth

To resolve the extended hot CGM, the PSF size of eROSITA limits the maximum redshift within which we should stack galaxies. With the stellar-to-halo mass relation from [Moster et al. \(2013\)](#), we infer the average dark matter halo mass and virial radius for a galaxy of a given stellar mass. We convert the virial radius to angular scale using the angular diameter distance as a function of redshift. As a reference, we take the size of the eROSITA PSF as $\theta = 30''$ ([Merloni et al. 2024](#); Sanders et al. in prep.) and calculate at which redshift the virial radius of the halo hosting the galaxy is equal to two and three times this value (i.e. $1'$ and $1.5'$), as listed in Table 1. For example, galaxies with $\log(M_*) = 10.75$ (similar to the Milky Way) have a resolved virial radius with two (three) eROSITA PSF up to $z = 0.21$ ($z = 0.13$). We then estimate the galaxy survey depth to ensure the galaxy sample's completeness is higher than 95% (we take r-band magnitude r_{AB} to evaluate). For example, to resolve the virial halo of $\log(M_*) = 10.75$ galaxies with two (three) eROSITA PSF, the galaxy survey needs to be deeper than $r_{AB} = 19.1(17.9)$.

By stacking samples up to $z_{2\times\text{PSF}}$, we obtain higher statistics to measure the luminosity of the CGM, and the survey depth should be deeper than $r_{AB} = 19.1$. Stacking samples up to $z_{3\times\text{PSF}}$, we obtain a better spatial resolution to measure the surface brightness profile of the CGM, and the survey depth can be shallower ($r_{AB} = 17.9$).

3.2. Choice of the parent galaxy surveys

There are numerous photometric and spectroscopic surveys since decades, such as Two Micron All Sky Survey (2MASS, [Skrutskie et al. 2006](#); [Bilicki et al. 2021](#)), VISTA Hemisphere Survey (VHS, [McMahon et al. 2013](#)), Wide-field Infrared Survey Explorer (WISE, [Wright et al. 2010](#)), SDSS ([Almeida et al. 2023](#)), skymapper ([Onken et al. 2019](#)), GAMA ([Driver et al. 2022](#)), Dark Energy Survey (DES, [Abbott et al. 2018](#)), Kilo Degree Survey (KiDS, [de Jong et al. 2017](#)), and DESI LS ([Dey et al. 2019](#)).

To make full use of the X-ray data at our disposal in the western Galactic hemisphere, the survey area is more important to us than depth. Therefore, we prefer wide-area surveys and do not consider deep but small fields such as HUDF (Hubble Ultra Deep Field, [Beckwith et al. 2006](#)), CDFS (*Chandra* Deep Field South; [Hsu et al. 2014](#)), and COSMOS (Cosmic Evo-

lution Survey, [Laigle et al. 2016](#)). Moreover, we prefer spectroscopic surveys that provide more accurate redshift measurements, stellar population, and galaxy classification. However, we also need to include photometric surveys to strive for large area and completeness before spectroscopic redshifts of bright galaxies ($r_{AB} < 20$) from 4MOST and DESI become available over the full sky ([DESI Collaboration et al. 2016](#); [de Jong et al. 2019](#); [Finoguenov et al. 2019](#))⁷.

In this work, we built our galaxy samples based on two surveys: SDSS DR7 ([Strauss et al. 2002](#)) and DESI LS DR9 ([Dey et al. 2019](#)), as listed in Table 2. SDSS DR7 provides enough statistics to study the CGM around galaxies within $z = 0.2$. LS DR9 is currently the most adequate photometric survey and we took it to build the galaxy sample out to $z_{2\times\text{PSF}}$ and down to $\log(M_*) = 9.5$, which provides the best statistics to detect the extended X-ray emission around galaxies.

3.2.1. SDSS DR7

The SDSS DR7 Main Galaxy Sample (MGS, $r_{AB} < 17.77$) covers $9,380 \text{ deg}^2$ of the sky and overlaps with the western Galactic hemisphere on about $4,010 \text{ deg}^2$ ([Strauss et al. 2002](#); [Abazajian et al. 2009](#)). The stellar mass of the galaxies is estimated by spectral energy distribution (SED) fitting and has a typical uncertainty of 0.1 dex ([Chen et al. 2012](#)). The spectroscopic redshift (z_{spec}) of the galaxy is estimated with an uncertainty of $\Delta z_{\text{spec}} < 10^{-4}$ ([Blanton et al. 2005](#)). The star-formation rate (SFR) of the galaxy is estimated by [Brinchmann et al. \(2004\)](#), which we take to model the XRB emission in Sect. 4.2.1. The galaxies hosting optical quasars identified with SDSS spectroscopy are not included in the SDSS MGS ([Strauss et al. 2002](#)). The galaxies hosting AGN in the SDSS MGS are identified as "AGN" or "composite" based on the BPT diagram, which we took to estimate the AGN emission, as described in Sect. 4.2.2 ([Baldwin et al. 1981](#); [Brinchmann et al. 2004](#)).

3.2.2. LS DR9 galaxy catalog

The LS DR9 ($r_{AB} < 23.4$) covers $14,000 \text{ deg}^2$ of the extragalactic sky and overlaps with the western Galactic hemisphere on about $9,340 \text{ deg}^2$ ([Dey et al. 2019](#)). We use the galaxy catalog from [Zou et al. \(2019, 2022\)](#)⁸. This catalog uses three optical bands (g, r, z) from CTIO/DECam and two infrared bands (W1, W2) from WISE photometry. This catalog includes galaxies with $r_{AB} < 23$, $S/N > 10$, and non-point-source-like morphology. The photometric redshift (z_{phot}) of the galaxy is estimated using a local linear regression algorithm (LePhare, [Arnouts et al. 1999](#); [Ilbert et al. 2006](#)). The uncertainty of z_{phot} is $\Delta z_{\text{phot}} = 0.01$. The stellar mass (M_*) of galaxies is derived from the spectral energy distribution (SED) fitting using theoretical stellar population synthesis models from [Bruzual & Charlot \(2003\)](#) at the photometric redshift. The uncertainty of $\log_{10}(M_*)$ is ~ 0.2 dex.

The nearby galaxies with a large extent on the sky need special treatment in the DESI legacy survey as summarized in the Siena Galaxy Atlas (SGA) catalog ([Moustakas et al. 2023](#)). We found that about 16,000 nearby galaxies in SGA are missing in the LS DR9 catalog. We added them to the catalog (see details in Appendix B).

⁷ In the longer term, Rubin ([Ivezić et al. 2019](#)) and Euclid ([Laureijs et al. 2011](#)) observatories will be excellent resources with exquisite depth and complete coverage of the southern hemisphere.

⁸ In this work, we use "LS DR9" to refer to the galaxy catalog from [Zou et al. \(2019, 2022\)](#).

Table 1: Constraints on the maximum redshifts of galaxies at different stellar masses to achieve > 95% completeness.

| $\log_{10}(M_*)$ [M_\odot] | $\log_{10}(M_h)$ [M_\odot] | R_h [kpc] | $z_{2\times\text{PSF}}$ | $z_{3\times\text{PSF}}$ | $r_{AB,2\times\text{PSF}}$ | $r_{AB,3\times\text{PSF}}$ | $z_{r_{AB}=17.77}$ |
|-----------------------------------|-----------------------------------|----------------|-------------------------|-------------------------|----------------------------|----------------------------|--------------------|
| 9 | 11.0 | 82 | 0.07 | 0.04 | 19.5 | 18.5 | <0.02 |
| 9.5 | 11.3 | 102 | 0.09 | 0.06 | 19.4 | 18.8 | 0.04 |
| 10 | 11.6 | 131 | 0.12 | 0.075 | 19.2 | 18.1 | 0.06 |
| 10.5 | 12.0 | 178 | 0.17 | 0.10 | 19.1 | 17.8 | 0.1 |
| 10.75 | 12.2 | 210 | 0.21 | 0.13 | 19.1 | 17.9 | 0.12 |
| 11.0 | 12.7 | 295 | 0.33 | 0.19 | 19.4 | 18.3 | 0.15 |
| 11.25 | 13.3 | 480 | 0.91 | 0.37 | 19.3 | 19.4 | 0.19 |
| 11.5 | 14.3 | 950 | >1 | >1 | 19.2 | 19.2 | 0.25 |

Notes. From left to right: Galaxy stellar mass, the corresponding average dark matter halo mass, the average halo radius, the redshift at which the projected halo radius equals two ($1'$) or three ($1.5'$) eROSITA PSF, the r-band survey depth required to achieve 95% completeness within $z_{2\times\text{PSF}}$ or $z_{3\times\text{PSF}}$ (we take $z = 0.4$ to calculate r_{AB} if $z_{2\times\text{PSF}}$ or $z_{3\times\text{PSF}}$ exceeds 0.4), and redshift within which galaxy survey with r-band survey depth $r_{AB} = 17.77$ achieves 95% completeness.

Table 2: Galaxy catalogs used in this work.

| Survey | A_{west} (deg ²) | Magnitude cut | N_{gal} | redshift | Reference |
|---------------|---------------------------------------|---------------|------------------|---------------|---------------------------------------|
| SDSS (DR7) | 4010 | $r < 17.77$ | 382428 | spectroscopic | Strauss et al. (2002) |
| DESI LS (DR9) | 9340 | $r < 23.4$ | 2387058 | photometric | Dey et al. (2019) |

Notes. A_{west} is the overlap area of the galaxy survey and the western Galactic hemisphere. The survey depth of each catalog is shown in column three. N_{gal} is the total number of galaxies stacked within the maximum redshift in the western Galactic hemisphere at different mass bins defined in Sect. 3.1. The calculation method of redshift and the relevant references are in the last two columns.

Table 3: Description of the galaxy samples.

| $\log_{10}(M_*/M_\odot)$ | | $M_{*,\text{med}}/M_\odot$ | $\log(M_{200\text{m,CEN}}/M_\odot)$ | | | redshift | | | FULL _{spec} | CEN | SAT |
|--------------------------|-------|----------------------------|-------------------------------------|-------|------|----------|------|------|----------------------|-------|-------|
| min | max | | 16% | med | 84% | min | max | med | N_g | N_g | N_g |
| 10.0 | 10.5 | 1.8×10^{10} | 11.5 | 11.75 | 12.1 | 0.01 | 0.06 | 0.05 | 11922 | 7956 | 3966 |
| 10.5 | 11.0 | 5.5×10^{10} | 11.8 | 12.1 | 12.6 | 0.02 | 0.10 | 0.08 | 45248 | 30825 | 14423 |
| 11.0 | 11.25 | 1.3×10^{11} | 12.2 | 12.7 | 13.1 | 0.02 | 0.15 | 0.12 | 34046 | 26099 | 7947 |
| 11.25 | 11.5 | 2.2×10^{11} | 12.6 | 13.1 | 13.6 | 0.03 | 0.19 | 0.15 | 24098 | 20342 | 3756 |

| $\log_{10}(M_{200\text{m}}/M_\odot)$ | | $M_{200\text{m,med}}/M_\odot$ | $\log(M_{*,\text{CEN,halo}}/M_\odot)$ | | | redshift | | | CEN _{halo} | SAT _{halo} |
|--------------------------------------|------|-------------------------------|---------------------------------------|-------|------|----------|------|------|---------------------|---------------------|
| min | max | | 16% | med | 84% | min | max | med | N_g | N_g |
| 11.5 | 12.0 | 5.5×10^{11} | 9.7 | 10.2 | 10.6 | 0.01 | 0.08 | 0.06 | 25368 | 903 |
| 12.0 | 12.5 | 1.7×10^{12} | 10.4 | 10.7 | 11.0 | 0.02 | 0.13 | 0.09 | 41301 | 4140 |
| 12.5 | 13.0 | 5.0×10^{12} | 10.8 | 11.0 | 11.2 | 0.02 | 0.16 | 0.12 | 30740 | 9145 |
| 13.0 | 13.5 | 1.6×10^{13} | 11.1 | 11.25 | 11.4 | 0.03 | 0.20 | 0.14 | 19889 | 9785 |
| 13.5 | 14.0 | 4.8×10^{13} | 11.2 | 11.4 | 11.6 | 0.03 | 0.20 | 0.16 | 8214 | 12537 |

| $\log_{10}(M_*/M_\odot)$ | | $M_{*,\text{med}}/M_\odot$ | redshift | | | FULL _{phot} | Isolated |
|--------------------------|-------|----------------------------|----------|------|------|----------------------|----------|
| min | max | | min | max | med | N_g | N_g |
| 9.5 | 10.0 | 5.5×10^9 | 0.01 | 0.09 | 0.07 | 95698 | 24280 |
| 10.0 | 10.5 | 1.8×10^{10} | 0.01 | 0.12 | 0.10 | 214286 | 50137 |
| 10.5 | 11.0 | 5.5×10^{10} | 0.02 | 0.17 | 0.14 | 415627 | 70348 |
| 11.0 | 11.25 | 1.3×10^{11} | 0.02 | 0.33 | 0.28 | 627757 | 50766 |
| 11.25 | 11.5 | 2.2×10^{11} | 0.03 | 0.40 | 0.35 | 324541 | 17983 |

Notes. For each table, from left to right, the columns are the stellar (halo) mass bin, median stellar (halo) mass, 16th percentile, median, and 84th percentile halo (stellar) mass of central galaxies, redshift bin, median redshift, and number of galaxies in the sample. Top: The FULL_{spec}, CEN, and SAT galaxy samples built from SDSS MGS. FULL_{spec} contains all galaxies within the stellar mass bin and redshift bin. We split the FULL_{spec} sample into central (CEN) or satellite (SAT) galaxy samples according to the group finder algorithm ([Tinker 2021](#)). Middle: The CEN_{halo} and SAT_{halo} sample of central galaxies binned in halo mass, built from SDSS MGS and is based on the group finder algorithm ([Tinker 2021](#)). Bottom: The FULL_{phot} and isolated galaxy samples built from DESI LS DR9. The FULL_{phot} contains all galaxies within the stellar mass bin and redshift bin. We select the isolated sample with the algorithm defined in Appendix. D.

3.3. The galaxy samples

All galaxy samples in this work are built to be approximately volume-limited. We outline their key properties and what we use them for. Five galaxy samples were selected from the SDSS MGS spectroscopic galaxy catalog:

- FULL_{spec} sample (Sect. 3.4.1): It includes all galaxies in the stellar mass range $10.0 < \log(M_*) < 11.5$ and spectroscopic redshift $0.01 < z_{\text{spec}} < 0.19$ (top panel of Table 3). It includes centrals and satellites. Therefore, we stack at the position of both centrals and satellites. We use this sample to help interpret the satellite boost bias (Sect. 5). We do not use this sample to derive the X-ray emission from the hot CGM.
- CEN sample (Sect. 3.7): It aims to include only central galaxies from the FULL_{spec} sample. The central galaxies are identified by the halo-based group finder with a misclassification possibility of about 1% (Tinker 2021). We use this sample to measure the X-ray surface brightness profiles of the hot CGM.
- SAT sample (Sect. 3.7): It includes only satellite galaxies from the FULL_{spec} sample. We use this sample to estimate the contamination from the misclassified central galaxies in the CEN sample.
- CEN_{halo} sample (Sect. 3.7): It aims to include only central galaxies selected in the halo mass range $\log M_{200\text{m}} = 11.5 - 14.0$ (middle panel of Table 3). The halo mass is estimated by the halo-based group finder algorithm (Tinker 2021). We use this sample to measure the X-ray surface brightness profiles of the hot CGM at different halo masses.
- SAT_{halo} sample (Sect. 3.7): It includes only satellite galaxies selected by the halo mass from the FULL_{spec} sample. We use it to estimate the contamination from the misclassified central galaxies for the CEN_{halo} sample.

Two galaxy samples are selected from DESI LS DR9 photometric galaxy catalog:

- FULL_{phot} sample (Sect. 3.4.2): It contains all galaxies in the stellar mass range $9.5 < \log(M_*) < 11.5$ and photometric redshift $0.01 < z_{\text{phot}} < 0.40$ (bottom panel of Table 3). The sample includes both centrals and satellites. Covering a larger area than SDSS, their stacked profiles will yield the highest signal-to-noise ratio (S/N).
- Isolated sample (Appendix. D): It includes galaxies selected from FULL_{phot} that live in under-dense environments. The sample has a high purity but a low completeness of isolated galaxies. It supplements the CEN samples and enables measurements of the total X-ray surface brightness profile at lower stellar mass.

3.4. Building of the Full_{spec} sample from the SDSS DR7 and the Full_{phot} sample from the LS DR9 galaxy catalogs

3.4.1. Full_{spec} galaxy sample

We selected galaxies with stellar mass $10.0 < \log(M_*) < 11.5$ from SDSS MGS because outside this range, the galaxy samples are too small, and identifying the central galaxy is hard. We split the galaxies into four stellar mass bins as listed in Table 3. We name the $\log(M_*) = 10.5 - 11.0$ bin as the "MW-mass" bin, the $\log(M_*) = 11.0 - 11.25$ bin as the "M31-mass" bin, and the $\log(M_*) = 11.25 - 11.5$ bin as the "2M31-mass" bin⁹.

⁹ The MW-mass, M31-mass, and 2M31-mass galaxies are defined only by the stellar mass, no extra selection is made on, for example, SFR or galaxy morphology

The maximum redshift is selected to ensure the sample is >95% complete, namely being approximately volume-limited. Considering the fact that the hot CGM of very local galaxies may extend across a large area over the sky and be susceptible to inaccurate background subtraction, we leave them for future studies. We take minimum redshift $z_{\text{min}} = 0.01 - 0.03$ for galaxy samples at different M_* bins. We obtain 115,314 galaxies in the FULL_{spec} sample.

3.4.2. Full_{phot} galaxy sample

We select the galaxies with $9.5 < \log(M_*) < 11.5$ from the LS DR9 catalog. We split the galaxy sample into five stellar mass bins as listed in Table 3. For the galaxy with both z_{spec} and z_{phot} measurements, we take z_{spec} . Constrained by the PSF of eROSITA, we take different maximum redshifts ($z_{2 \times \text{PSF}}$) for each mass bin (see Table 3). Similar to FULL_{spec}, we take minimum redshift $z_{\text{min}} = 0.01 - 0.03$ for galaxy samples at different M_* bins. Finally, we obtained the 1,677,909 galaxies that constitute the FULL_{phot} sample.

3.5. Galaxy-halo connection

Galaxies reside in various environments, ranging from voids to superclusters. To interpret the stacked measurement of the hot CGM without ambiguity, we need to relate one galaxy sample to its environment, that is, its host dark matter halo distribution (see a review from Wechsler & Tinker 2018), as discussed in Comparat et al. (2022). Within a dark matter halo, the central galaxy, which is the most massive one, is thought to reflect the properties of the halo (i.e., the halo mass), and profoundly influences the hot CGM of the satellites; on the other hand, there is a loose relation between satellite galaxies and the halo properties.

Studies of galaxy clustering and galaxy-galaxy lensing constrained the galaxy-halo connection using SDSS galaxy survey at low redshift (Zehavi et al. 2011; Zu & Mandelbaum 2016), the GAMA galaxy survey at slightly higher redshifts (Linke et al. 2022), and deeper spectroscopic surveys including COSMOS and CFHTLenS/VIPERS at even higher redshifts (Leauthaud et al. 2012; Coupon et al. 2015). Overall, a double power-law with a 0.15 dex scatter can describe the stellar-to-halo relation for central galaxies well. There is no tight relation between the stellar mass of the satellite galaxy and its host halo mass. The fraction of galaxies that are satellites of a more massive halo (f_{sat}) decreases with increasing stellar mass; for the MW-mass galaxies, f_{sat} is about 30%.

3.6. Contamination by the satellite boost and X-ray sources in satellite galaxies

The existence of satellite galaxies influences the stacking in two ways (see top panel of Fig. 1 for an illustration):

- Satellite boost: Including satellite galaxies in the stacking sample would wrongly boost the X-ray emission. A satellite galaxy would be located in a more massive dark matter halo compared to a central galaxy with the same stellar mass. Therefore, the stacked X-ray emission around satellite galaxies is boosted by the hotter and brighter emission of the plasma from the more massive (parent) dark matter halo. This extra emission should not be attributed to the satellite galaxy. The bright X-ray emission from the nearby, more massive central galaxy flattens the X-ray profile of the satellite (see the filled curves in the bottom panel of Fig. 1,

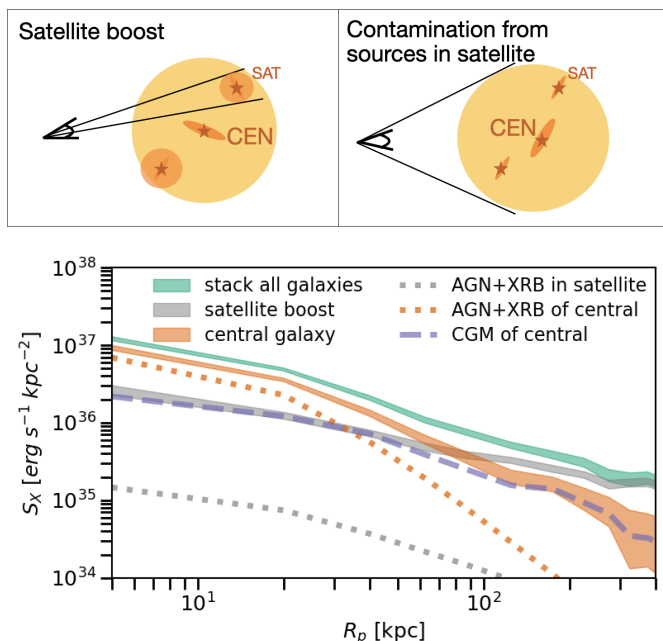


Fig. 1: Illustration of contamination to the stacking from the satellite boost bias and sources in the satellites (top). An illustration of the X-ray surface brightness profiles of different components is also shown in the bottom panel. The X-ray surface brightness profile of central galaxies that we are interested in (orange band) is obtained by subtracting the satellite boost (or misclassified central, gray band) from the stacking of all (or central) galaxies (green band). The hot CGM X-ray emission of the central galaxy (purple dashed line) is modeled by subtracting the X-ray emission from the X-ray sources in satellite galaxies (gray dotted line) and central galaxies (orange dotted line) from the X-ray surface brightness profile of central galaxies (orange band).

more discussion in Sect. 5.2). To avoid the satellite boost, we stack only central galaxies to measure the X-ray emission around galaxies. The misclassification of a satellite galaxy as a central galaxy causes a satellite boost in the stack, we model their contamination in Sect. 4.3. In the article we interchangeably use ‘misclassified central’ (the cause) or ‘satellite boost’ (the effect) to describe this feature.

- Contamination from sources in satellites: Even when stacking around central galaxies, the X-ray emission from non-CGM X-ray sources (AGN or XRB) in satellite galaxies is unavoidably stacked and contaminates the X-ray emission from the hot CGM (see the dashed lines in the bottom panel of Fig. 1). We will model the contamination by the X-ray sources in the satellite galaxies in Sect. 4.2.3.

In summary, the accurate selection of central galaxies and weeding out of the satellite contaminants represent a crucial element of our analysis. We discuss how this can be achieved for the spectroscopic samples at our disposal in the following sections. The discussion of the photometric sample is in Appendix. D.

3.7. Building of the CEN, SAT, CEN_{halo} and SAT_{halo} samples from SDSS MGS

An unbiased selection of central galaxies requires accurate measurement of galaxy redshifts, the typical redshift uncertainty needs to be at least smaller than 10^{-4} . For the SDSS MGS, it is

possible to define a central galaxy sample, and different schemes exist to select central galaxies. A commonly used approach is the friends-of-friends (FoF) algorithm: galaxies are identified as a group according to the linking lengths, and within each group, the brightest galaxy is defined as the central galaxy (Crook et al. 2007; Robotham et al. 2011; Tempel et al. 2016). An alternative method is to define the locally brightest galaxies as central galaxies and other galaxies falling within a certain distance around them are satellites (Anderson et al. 2015; Comparat et al. 2022). More involved approaches include self-calibrated halo-based group finding (Yang et al. 2005; Tinker 2022), group finder with galaxy weighting (Abdullah et al. 2018), Bayesian group finder based on marked point processes (Tempel et al. 2018).

Here, the self-calibrated halo-based group finding algorithm is applied to the SDSS MGS to classify galaxies as centrals or satellites and estimate their halo mass (Tinker 2021, 2022). The halo-based group finding algorithm searches for galaxy groups within the same dark matter halos and identifies the central galaxy. The algorithm is calibrated by the mock galaxy distributions and is further self-calibrated using the observations, including the galaxy clustering measurements, lensing, and satellite luminosity measurements. The algorithm assigns halos to galaxies by comparing the catalog to complementary data (Tinker 2021). The algorithm’s performances are excellent: the halo masses of either star-forming or quiescent central galaxies agree well with the halo masses estimated from weak-lensing observation. The clustering properties, halo occupation distribution (HOD), and $M_h - M_*$ relation of star-forming or quiescent galaxies are also well reproduced (Tinker 2022). The chance of misclassified central is about 1%.

For each galaxy in the SDSS MGS, its probability as central or satellite (P_{sat} , we use the recommended $P_{\text{sat}} = 0.5$ as a boundary), and its host halo mass is provided in Tinker (2021).

3.7.1. Central and satellite galaxy samples in stellar mass bins (CEN and SAT)

The central galaxy sample (CEN) and satellite galaxy sample (SAT) selected from the SDSS MGS in stellar mass bins are listed in Table 3. In total, we have 85,222 central galaxies and 30,092 satellite galaxies.

3.7.2. Central and satellite galaxy samples in halo mass bins (CEN_{halo} and SAT_{halo})

There is a large scatter in the stellar-to-halo-mass relation, which introduces the ‘inversion problem’¹⁰. Therefore, we also stack galaxies selected in halo mass. With halo mass assigned to each galaxy in the SDSS MGS by the group finder algorithm, we can study how the $M_{\text{halo}} (M_{200\text{m}})$ ¹¹ is related to the X-ray emission of galaxies directly. We define a halo mass-selected central galaxy sample (we name it as CEN_{halo} sample) by splitting it into five logarithmic bins in the range $\log M_{200\text{m}} = 11.5 - 14.0$ of 0.5 dex

¹⁰ If sample A, selected based on stellar mass, has the same mean halo mass as sample B, selected based on halo mass, the galaxies in the two samples will be different (i.e., the stellar mass and SFR (see Fig.2 in Moster et al. 2020)). This difference arises because the criteria used to select the galaxies are different. The inversion problem refers to the phenomenon where different selection criteria can lead to different sets of galaxies. Consequently, this can result in drawing different conclusions from samples A and B.

¹¹ The M_{halo} provided in the catalog Tinker (2021) is $M_{200\text{m}}$, the mass within the radius where the mean interior density is 200 times the background universe density.

each, see Table 3. We set the maximum redshift for each CEN_{halo} bin at the redshift where its median stellar mass completeness is at 90% for a magnitude cut $r_{AB} = 17.77$. We have 125,512 central galaxies in the CEN_{halo} sample and 36,510 satellite galaxies in the SAT_{halo} sample.

By selecting the CEN and CEN_{halo} samples respectively, we manage to account for the scatter in the SHMR. In Table 3, we list the 16th percentile, median, and 84th percentile $M_{200\text{m}}$ (M_*) of each M_* ($M_{200\text{m}}$) bin in the CEN (CEN_{halo}) sample. Although a stellar mass bin in the CEN sample and a halo mass bin in the CEN_{halo} sample may have similar median stellar mass or halo mass, the included galaxies are not the same. For example, the $\log(M_*) = 10.5 - 11.0$ bin of CEN has a broader distribution of $M_{200\text{m}} \approx 11.8 - 12.6$, compared to the $\log(M_{200\text{m}}) = 12.0 - 12.5$ bin of CEN_{halo} .

4. Models

Given the complexity of the galaxy-halo relation, the possible contaminations from satellite galaxies, and unresolved X-ray sources (XRB and AGN), a robust interpretation of the stacking results requires reliable models to control all of the above effects.

In this section, we introduce a mock galaxy catalog built from simulations to help control the properties of galaxy samples in Sect. 4.1. The X-ray emission from unresolved AGNs and XRBs in the stacked galaxies and satellite galaxies is modeled in Sect. 4.2. The contamination from the misclassified central galaxy in the group finder is modeled in Sect. 4.3. We summarize how the models are used in Sect. 4.4.

4.1. Mock galaxy catalog

We built a mock catalog to help characterize and gain insights into the designed galaxy samples. We used the Uchuu simulation (Ishiyama et al. 2021) and its UNIVERSEMACHINE galaxy catalog (Behroozi et al. 2019). The Uchuu simulation is a suite of ultra-large cosmological N-body simulations to construct the halo and sub-halo merger trees in a box of $2.0h^{-1}\text{Gpc}$ side-length, with mass resolution of $3.27 \times 10^8 h^{-1} M_{\odot}$, using the cosmological parameters obtained by Planck (Planck Collaboration et al. 2020; Ishiyama et al. 2021). The galaxy model aptly reproduces the stellar mass function and the separation between red-sequence and blue-cloud galaxies. We created a full-sky light cone following the method from Comparat et al. (2020).

We empirically calibrated the relation between stellar mass and K-band absolute magnitude (and its scatter) as a function of redshift using observations from SDSS, KIDS+VIKING, GAMA (for redshift smaller than 0.75) and COSMOS (for higher redshifts) (Ilbert et al. 2013; Almeida et al. 2023; Kuijken et al. 2019; Driver et al. 2022). With these relations, we assign an absolute K-band magnitude to each simulated galaxy using the stellar mass prediction from UNIVERSEMACHINE. Then, we search the observed data sets for the nearest neighbor to each simulated galaxy in redshift and K-band. The set of observed broadband magnitudes (particularly the r-band) obtained with the match is assigned to the simulated galaxy. We find that the galaxy painting process is faithful to the observed galaxy population up to redshift ~ 0.5 ¹². The light cone well reproduces the observed K-

¹² Beyond the redshift of 0.5, systematic effects due to the observed samples used (less accurate photometric redshifts in KIDS, small area subtended by COSMOS) lessen the quality of the mock catalog. However, we do not use the mock catalog in this redshift regime.

band and r-band luminosity functions from GAMA (or SDSS). We can thus apply the magnitude limit used in this work to the light cone. In the light cone, central (as the brightest galaxy) and satellite galaxies are defined accurately.

We built a mock SDSS MGS catalog from the light cone to $z=0.45$. We apply the magnitude cut $r_{AB} < 17.77$ and add a Gaussian distributed $z_{\text{error}} = 10^{-4}$ and $M_{\text{error}} = 0.01$ dex to the accurate ones from the light cone. We use the mock SDSS MGS catalog to evaluate the satellite galaxy distribution.

4.2. Models for AGN and XRB emission

The PSF and sensitivity of eROSITA prevent us from resolving all point sources at the redshift of the galaxies we stack. Therefore, to infer what fraction of the measured X-ray emission comes from the hot CGM, in this section we opt for an empirical model to predict the XRB X-ray emission based on the stellar mass and SFR of galaxies (Sect. 4.2.1). For the AGN, we opt for an observation-based approach (Sect. 4.2.2 and Appendix. C). The X-ray emission of XRB in the satellite galaxies is modeled using the mock catalog (Sect. 4.2.3). With the predicted luminosity of the XRB and AGN, we normalize the PSF to obtain their X-ray surface brightness profiles¹³.

4.2.1. Model for XRB

The X-ray luminosity of XRB in the 2-10 keV band ($L_{2-10\text{keV}}$) scales with the SFR and M_* of host galaxies (Aird et al. 2017; Lehmer et al. 2019). For the CEN and CEN_{halo} samples, we predict the $L_{2-10\text{keV}}$ and estimate its uncertainty using the model in Aird et al. (2017) (see Eq.5 of Aird et al. (2017)). We also use the empirical model compiled by Lehmer et al. (2019) to estimate the XRB luminosity and obtain consistent results. The selection of the XRB model does not affect our conclusions. We convert $L_{2-10\text{keV}}$ to the X-ray luminosity in 0.5-2 keV (L_{XRB}) by assuming an absorbed power law with a photon index of 1.8, and with column density fixed at $N_H = 2.3 \times 10^{20} \text{cm}^{-2}$, the mean N_H of the stacked area.

4.2.2. Model for AGN

To model the AGN emission for the CEN and CEN_{halo} samples, we consider the galaxies identified as "AGN" or "composite" using the BPT diagram applied to the SDSS MGS central galaxies and name these galaxies as CENAGN sample (Baldwin et al. 1981; Brinchmann et al. 2004). Depending on the stellar mass, $f_{\text{AGN}} = 8-18\%$ of the galaxies in the CEN sample were selected as CENAGN (see Table C.1). We stacked the galaxies in the CENAGN sample, masking all detected X-ray sources to calculate the maximum X-ray emission from unresolved AGN and XRB as described in Appendix. C. We estimated the AGN emission (L_{AGN}) as the residual emission after subtracting the XRB emission. Under the assumption of no other galaxies hosting AGN, the lower limit of the average AGN contamination in the CEN

¹³ We notice XRB are located around the galaxy disk and its surface brightness profile may not be PSF-like. To test if it has an impact, we do the following. We assume XRB distribute as a Sérsic profile: $S_X = S_{X,0} \exp[-(r/r_{50})^{1/n}]$, where r is the distance to galaxy center, r_{50} is the half-light radius of the galaxy and n is the Sérsic index. We conservatively take $n = 4$ and $r_{50} = 10 \text{kpc}$ (see Shen et al. 2003, Fig. 11). We convolve the Sérsic profile with the PSF and find the difference to the PSF to be negligible ($< 5\%$). Therefore, we use only the PSF to model the XRB surface brightness profile.

sample is $L_{\text{AGN}} \times f_{\text{AGN}}$. To be conservative, we take the upper limit of AGN contamination as $2 \times L_{\text{AGN}} \times f_{\text{AGN}}$; this accounts for (obscured) X-ray AGN not being identified as AGN or composite in the SDSS spectra. We repeated the procedure for the CEN_{halo} sample to estimate the AGN contamination there (see the discussion in Appendix. C). We find that the unresolved AGN contamination is comparable to the XRB emission at the stellar mass (or halo mass) ranges we focus on. Our AGN model is consistent with the empirical AGN model derived in [Comparat et al. \(2019, 2023\)](#).

4.2.3. XRBs in satellite galaxies

The AGN and XRBs in the satellites would contaminate the hot CGM emission attributed to the central galaxy. We took the mock SDSS MGS catalog to evaluate the satellite galaxy distribution. For each stacked galaxy in the CEN sample, we selected the galaxy with similar stellar mass (difference smaller than 0.1 dex) and redshift (difference smaller than 0.01) in the mock catalog. We counted the number of satellite galaxies and the projected distances of the satellites to the mock central galaxy. The AGN population in satellite galaxies is unclear; there could be 0-20% satellite galaxies hosting AGN ([Comparat et al. 2023](#)). We assume the AGN contamination in the satellite galaxies is negligible after applying masks. We estimate the XRB emission of the satellites according to properties (M_* and SFR) from the mock catalog, as in Sect. 4.2.1. We sum and average the XRB emission in satellites as a function of distance to the central galaxy.

We find the total X-ray luminosity of unresolved XRBs in satellites is about 8% (19%, 37%, 66%) of the XRB in the stacked central galaxies for the four M_* bins in the CEN sample, respectively. Therefore, the model of unresolved point sources in satellites is necessary, especially for massive galaxies. We repeat the same procedure above for the CEN_{halo} sample.

4.3. Model for misclassified central galaxies

The satellite galaxies might be misclassified as central in the group finder, with a chance of $<1\%$ ([Tinker 2021](#)). In the case of stellar mass selection (CEN), since satellites are hosted by more massive (brighter in X-ray) haloes, the contamination can not be ignored. Here, we consider the 1% satellite galaxies in the CEN (or CEN_{halo}) sample and model their contamination. We stack galaxies and measure the X-ray emission in the SAT (or SAT_{halo}) sample ($S_{\text{X,SAT}}$). We rescale the X-ray profiles of CEN ($S_{\text{X,CEN}}$) as $(S_{\text{X,CEN}} - 1\%S_{\text{X,SAT}})/99\%$. The rescaled X-ray luminosity of CEN drops by about 5%.

4.4. Application of the models

The models were applied to the CEN and CEN_{halo} samples as follows:

- Modelling the misclassified central. We follow the procedure in Sect. 4.3 to rescale the measured X-ray surface brightness profile of CEN and CEN_{halo} samples. This step corrects for the contamination from the 1% misclassified central (namely satellite) galaxies.
- Modelling the unresolved AGN and XRB in central galaxies. We assume the mean X-ray profile of unresolved point sources to be PSF-like. We estimate the X-ray luminosity of unresolved AGN in the CEN and CEN_{halo} samples following the procedure in Sect. 4.2.2. We estimate the X-ray luminosity of XRB in the stacked central galaxies with the

empirical model described in Sect. 4.2.1. We sum up the X-ray luminosity of unresolved AGN and XRB to normalize a PSF profile accordingly.

- Modelling the unresolved XRB in satellite galaxies. We consider that the satellite galaxies located within the halo of stacked galaxies contaminate the hot CGM. We estimate the XRB luminosity of the satellite galaxies following the procedure in Sect. 4.2.3. The X-ray profile is predicted using the satellite distribution from the mock catalog.

From the stacked surface brightness profile ($S_{\text{X,stack}}$) with X-ray point sources masked (see Sect. 2.2) and misclassified centrals corrected (see Point 1 above), we obtain the surface brightness of the CGM by subtracting the modeled contamination ($S_{\text{X,AGN+XRB+SAT}}$, Points 2 and 3 above): $S_{\text{X,CGM}} = S_{\text{X,stack}} - S_{\text{X,AGN+XRB+SAT}}$.

5. X-ray surface brightness profile around galaxies from the FULL and SAT samples

In this section, we present the measured X-ray surface brightness profiles of $\text{FULL}_{\text{phot}}$ (or $\text{FULL}_{\text{spec}}$) samples (Sect. 5.1). We quantify the satellite boost bias in Sect. 5.2 and apply it to model the misclassified centrals as described in Sect. 4.3.

5.1. X-ray surface brightness profile of $\text{FULL}_{\text{phot}}$ sample

Stacking the $\text{FULL}_{\text{spec}}$ or $\text{FULL}_{\text{phot}}$ sample without masking any detected X-ray sources introduces the least uncertainty and bias (from X-ray data reduction or galaxy sample compiling) to the results; the measurement is reproducible. The surface brightness profiles of the $\text{FULL}_{\text{phot}}$ samples in $\log(M_*) = 10.0 - 10.5$, MW-mass and M31-mass (after subtracting the background) are shown in Fig. 2.

We notice the significant improvement of the statistics by comparing the X-ray surface brightness profile to the one measured by stacking 16,142 galaxies with $\log(M_*) = 10.4 - 11.0$ and $z_{\text{spec}} = 0.05 - 0.3$ selected from the GAMA catalog using the eFEDS X-ray data ([Comparat et al. 2022](#)). The X-ray surface brightness profiles obtained here have a high S/N. These high-significance measurements benefit from a large number of sources available within the large area considered in this work and covered by the eROSITA observations.

Due to the satellite boost bias we described in Sect. 3.6, the satellite galaxies located in more massive dark matter halo strongly influence the profiles shown in Fig. 2, resulting in the stacked X-ray emission extending to about 1-2 Mpc (about 5-10 times of R_{vir} of galaxies). The X-ray sources contributing to these stacks include AGN, XRB, and hot gas emission: intra-cluster medium (ICM), intra-group medium (IGrM), and CGM¹⁴ from central and satellite galaxies in different massive halos. The interpretation of these measurements remains complex, and future simulation and modeling efforts will enable an unambiguous interpretation of all the signals present in these measurements. In Sect. 5.2, we briefly discuss the different X-ray surface brightness profiles around central and satellite galaxies. However, we leave the elaboration of an accurate satellite boost model that will enable the complete extraction of the information in these stacks with high S/N values for future studies ([Shreeram et al. in prep.](#)).

¹⁴ Hereafter in our work, we use CGM to denote the medium within the virial radius of the galaxy, regardless if the galaxy is in group or cluster.

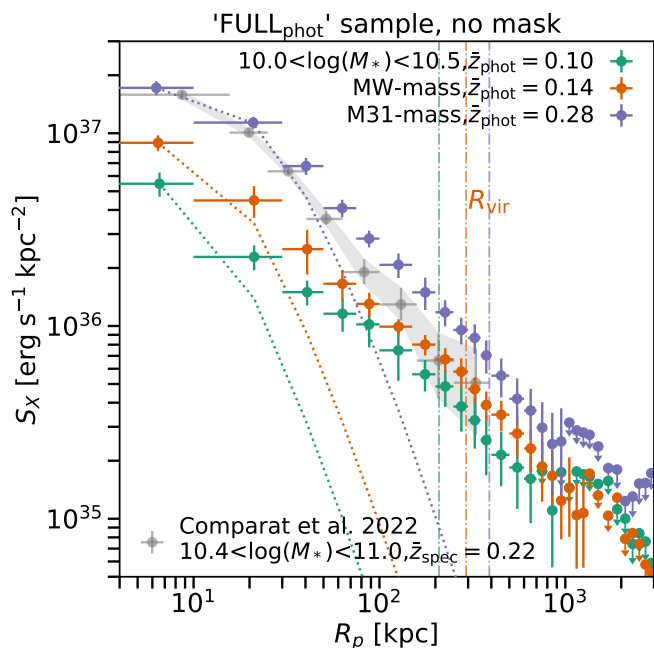


Fig. 2: X-ray surface brightness profiles of the $\text{FULL}_{\text{phot}}$ sample after subtracting background, without masking sources. The results are divided into galaxy mass bins $\log(M_*) = 10.0 - 10.5$, $10.5 - 11.0$ (MW-mass), and $11.0 - 11.025$ (M31-mass) as labeled. The dotted line is the PSF of eROSITA, and the vertical dash-dotted line denotes the average virial radius of stacked galaxies. The X-ray emission comprises all effects mentioned in Sect. 3.6, limiting its interpretability regarding CGM emission. The X-ray surface brightness profile measured by stacking 16,142 galaxies with $\log(M_*) = 10.4 - 11.0$ and $z_{\text{spec}} = 0.05 - 0.3$ is plotted in gray (Comparat et al. 2022). The galaxy sample in Comparat et al. (2022) contains a complete population of AGN (while our $\text{FULL}_{\text{phot}}$ does not contain sources that appear point-like in the legacy survey photometry) and has a broader PSF due to its higher mean redshift. So we expect the previous measurement to agree with the FULL MW-mass at large separation but to be brighter in the center.

5.2. Untangle the X-ray emission from satellite and central galaxies in $\text{FULL}_{\text{spec}}$ sample

The satellite boost biases the results of the stacking experiment. In this section we use the central/satellite galaxy classification of the SDSS spectroscopic sample and stack the X-ray emission around galaxies in CEN and SAT samples to study the difference and to untangle the X-ray surface brightness profile of central galaxies from the stacking of $\text{FULL}_{\text{spec}}$.

The comparison of the X-ray surface brightness profile of $\text{FULL}_{\text{spec}}$, CEN, and SAT sample is plotted in Fig. 3, taking the M31-mass bin as an example. As expected, galaxies with the same M_* but classified as satellites or centrals have different X-ray surface brightness profiles. The satellite galaxy, residing in a more massive dark matter halo, has its X-ray emission boosted by the emission from virialized gas of the larger halo they reside in, from nearby centrals and other satellite galaxies. Consequently, the X-ray surface brightness profiles of the satellite galaxies appear to be more extended and brighter than those of the central.

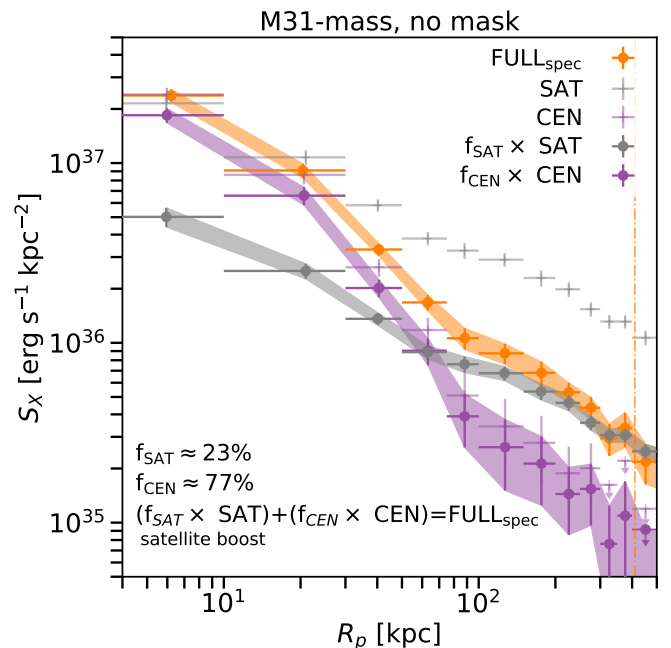


Fig. 3: Observed mean X-ray surface brightness profile of galaxies in M31-mass bin of $\text{FULL}_{\text{spec}}$ sample and the profiles after splitting $\text{FULL}_{\text{spec}}$ sample to central (CEN) or satellite (SAT) galaxies. We scale the observed surface brightness profiles of CEN and SAT according to the number ratio of galaxies, namely, $f_{\text{SAT}} = N_{\text{g,SAT}}/N_{\text{g,FULL}_{\text{spec}}}$ and $f_{\text{CEN}} = N_{\text{g,CEN}}/N_{\text{g,FULL}_{\text{spec}}}$. The vertical dash-dotted line denotes the average virial radius of M31-mass galaxies in the $\text{FULL}_{\text{spec}}$ sample.

We rescale the profile of central or satellite galaxies by their number ratio. Namely, we multiply the mean profile of central or satellite galaxies by $N_{\text{CEN}}/N_{\text{g}}$ or $N_{\text{SAT}}/N_{\text{g}}$, respectively. These rescaled profiles of centrals and satellites, compared to the $\text{FULL}_{\text{spec}}$ sample, are plotted in Fig. 3. We find that, beyond 100 kpc, the emission from satellite galaxies dominates over the central galaxy and determines the profile shape of the $\text{FULL}_{\text{spec}}$ sample, as we had argued. This proves the necessity of selecting central galaxies to study how a galaxy modulates the properties of its CGM. On the other hand, we can use the rescaled profiles to untangle the emission in $\text{FULL}_{\text{spec}}$ sample and model the influence of the misclassified central galaxy, as we discussed in Sect. 4. Finally, we go on to focus on the CEN and CEN_{halo} samples where the satellite boost bias that hampers the interpretation of the full stacks is minimized.

6. The circumgalactic medium of central galaxies selected in stellar mass and halo mass

In this section, we mask all identified X-ray point sources so that the emission from the hot gas component becomes more discernible. The observed surface brightness profiles of the CEN and CEN_{halo} samples are presented in Sect. 6.1. The X-ray emission from the hot CGM emission is modeled (following the steps in Sect. 4.4) and presented in Sect. 6.2.

6.1. The X-ray surface brightness profiles

The X-ray surface brightness profiles up to R_{vir} of the CEN sample in MW-mass, M31-mass, and 2M31-mass are plotted in the

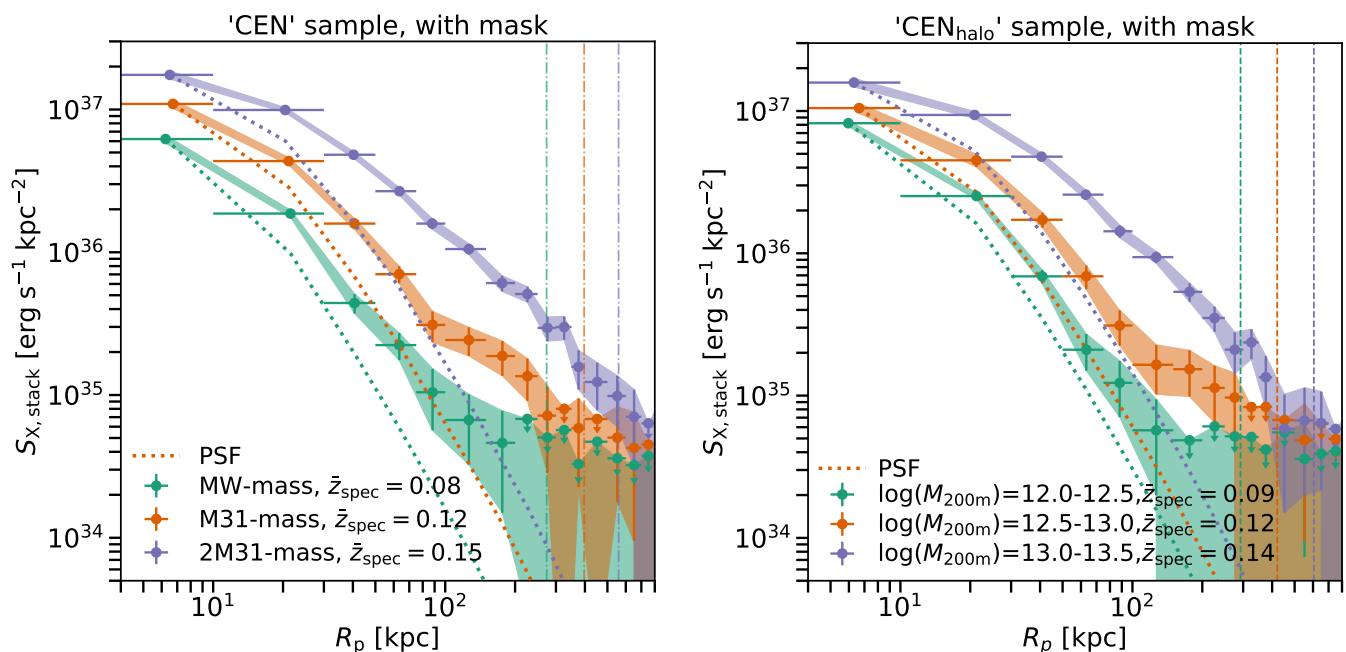


Fig. 4: Mean X-ray surface brightness profiles of central galaxies (with a magnitude limit of $r_{\text{AB}} < 17.77$) after subtracting background and masking X-ray point sources, for galaxies with $\log(M_*) = 10.5 - 11.0$ (MW-mass), $11.0-11.25$ (M31-mass), and $11.25-11.5$ (2M31-mass) shown on the left. The X-ray emission comprises unresolved point sources and hot gas. \bar{z} is the median redshift of galaxies in each mass bin. The dotted lines are the PSF of eROSITA. The vertical dash-dotted lines are the virial radius at different stellar mass bins correspondingly. Right panel shows the mean X-ray surface brightness profiles of central galaxies with $\log(M_{200\text{m}}) = 12.0 - 13.5$ after subtracting background and masking X-ray point sources.

left panel of Fig. 4. The X-ray emission detected here is the sum of unresolved point sources and hot gas emission from the stacked central galaxies (plus their satellite galaxies) within R_{vir} . We find that the X-ray surface brightness increases with stellar mass. The extended nature of the emission can be visually identified by comparing the X-ray surface brightness profile to the PSF of eROSITA (dotted line). Flatter profiles than the PSF are observed beyond 30 kpc for MW-mass and more massive galaxies (left panel of Fig. 4). The profile becomes more extended with increasing stellar mass. For the MW-mass, M31-mass, and 2M31-mass galaxies in the CEN sample, the X-ray emission is detected within the virial radius of galaxies with $S/N \approx 3.1, 4.7, 8.3$.

The X-ray surface brightness profiles of galaxies with $\log(M_{200\text{m}}) = 12.0 - 13.5$ are plotted in the right panel of Fig. 4. The X-ray surface brightness increases with $M_{200\text{m}}$. Extended emission is detected around central galaxies in halos with $\log(M_{200\text{m}}) > 12.5$ with $S/N \approx 2.8, 5.3, 6.9$ for the three bins, respectively.

For the first time, we measure the extended X-ray emission up to the virial radius around the MW-mass and M31-mass central galaxies with a high S/N .

6.2. The hot CGM emission in MW-mass or more massive galaxies

The hot CGM profiles of MW-mass, M31-mass, and 2M31-mass central galaxies are presented in Fig. 5. The modeled X-ray emission from AGN, XRB, and misclassified central galaxies (plotted in orange) contributes to most of the emission within 20 kpc and is less extended than the detected X-ray emission (green dots). The X-ray emission from the hot CGM (purple

band) is detected within R_{vir} with $S/N \approx 1.7, 3.9, 7.7$ for MW-mass, M31-mass and 2M31-mass galaxies.

We fit the β model (Eq. 3) to the hot CGM X-ray profile to obtain an analytical description of the results. The fit results are reported in Table 4. We get $\beta \approx 0.43$ for MW-mass galaxies and $\beta \approx 0.37$ for M31-mass and 2M31-mass galaxies. $\log(S_{X,0})$ increases with M_* , while r_c is poorly constrained, limited by the uncertainty of modeled AGN, XRB, and misclassified central galaxies emission.

The results for CEN_{halo} sample are presented in Fig. 6. The X-ray emission from the hot CGM is detected within R_{vir} with $S/N \approx 2.2, 4.9, 6.6$ for the halo mass bins $\log(M_{200\text{m}}) = 12.5 - 13.0, 13.0 - 13.5, \text{ and } 13.5 - 14.0$ respectively. The fit results of the β model are listed in Table 4. We get $\beta \approx 0.4$.

Prior to the publication of this work, the value of β had been measured in several nearby massive galaxies ($\log(M_*) \approx 11.5$), within $0.5R_{\text{vir}}$ with $\beta \approx 0.397 \pm 0.009$, which is consistent with our measurement¹⁵ (Li et al. 2017, 2018). The hot CGM density profile beyond $0.5R_{\text{vir}}$ is not well studied yet, as a result, the baryon budget stored in the hot CGM is poorly constrained by the X-ray observations (Li et al. 2018; Das et al. 2020, 2023). With our newly measured hot CGM density profile within R_{vir} , we describe how we estimated the baryon mass and fraction in Sect. 7.

¹⁵ Besides the β model, the exponential model is proposed to describe the inner hot CGM ‘corona’ of the Milky Way and nearby galaxies, $S_{X,\text{exp}} = S_{X,0}e^{-r/r_s}$, where r_s is the scale radius with a value of some kiloparsecs (Yao et al. 2009; Locatelli et al. 2024). Limited by the PSF of eROSITA, we can not resolve the sharp corona component.

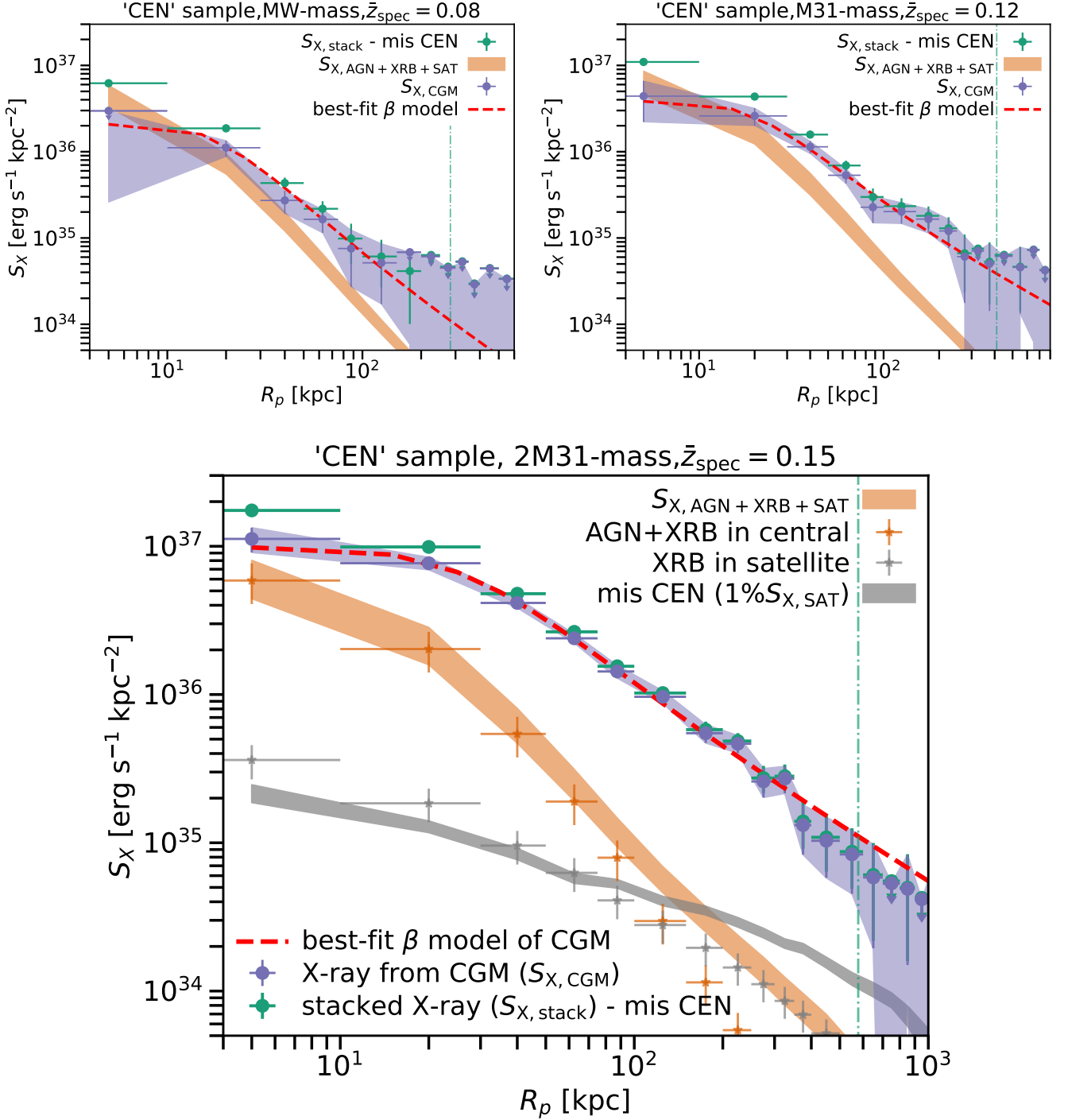


Fig. 5: Mean X-ray surface brightness profiles of central galaxies selected from SDSS in different M_* bins, after masking X-ray sources and correction of misclassified centrals (green points, $S_{X,\text{stack}}$), the total X-ray surface brightness of unresolved AGN and XRB in the stacked galaxies and satellites (orange band), and the X-ray surface brightness of the CGM (purple band, $S_{X,\text{CGM}}$) modeled by subtracting the unresolved AGN and XRB from the $S_{X,\text{stack}}$ (See Sect. 4.4 for details). The red dashed line is the best-fit of the CGM profile with a β model. The vertical dash-dotted line is the virial radius, R_{vir} . The top two panels are for MW-mass and M31-mass galaxies, and the bottom panel is for 2M31-mass galaxies. In the bottom panel, we further denote the X-ray surface brightness profiles of modeled unresolved AGN and XRB in the central galaxies (orange cross), XRB in the satellite galaxies (gray cross), and X-ray surface brightness profile of misclassified satellite (gray band).

7. The baryon budget

Based on the derived parameters of β models (in Sect. 6.2), we estimated the baryon mass and baryon fraction within R_{vir} of

central galaxies. The density profile of the hot CGM in the β

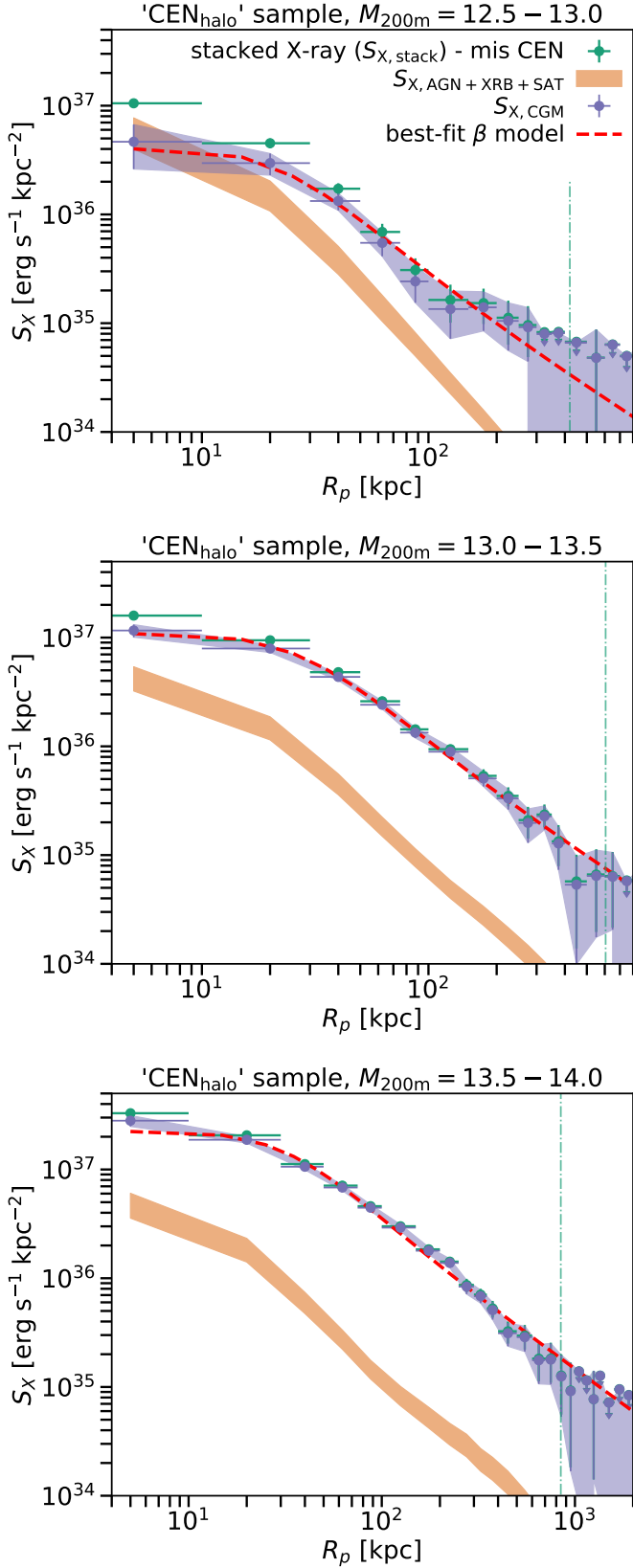


Fig. 6: Same as Fig. 5, but for galaxies selected in halo mass bins. From top to bottom, the X-ray surface brightness profiles for $M_{200m} = 12.5 - 13.0$, $13.0-13.5$, $13.5-14.0$.

model is then:

$$n(r) = n_0 \left[1 + \left(\frac{r}{r_c} \right)^2 \right]^{(-\frac{3}{2}\beta)} \quad [\text{cm}^{-3}], \quad (4)$$

Table 4: Best-fit parameters of β model for the X-ray surface brightness profiles of CGM for the CEN and CEN_{halo} samples.

| | MW-mass | M31-mass | 2M31-mass |
|------------------------------------------------------------|------------------------|------------------------|------------------------|
| β | $0.43^{+0.10}_{-0.06}$ | $0.37^{+0.04}_{-0.02}$ | $0.37^{+0.02}_{-0.01}$ |
| $\log(S_{X,0})$ [$\text{erg s}^{-1} \text{kpc}^{-2}$] | $36.7^{+1.4}_{-0.4}$ | $37.1^{+1.5}_{-0.4}$ | $37.3^{+0.1}_{-0.1}$ |
| r_c [kpc] | 6^{+9}_{-5} | 4^{+7}_{-3} | 10^{+3}_{-3} |
| χ^2 | 4.0 | 3.2 | 6.6 |
| d.o.f. | 5 | 8 | 10 |
| $\chi^2/\text{d.o.f.}$ | 0.8 | 0.4 | 0.7 |

| | $\log(M_{200m})$ | | |
|------------------------------------------------------------|------------------------|------------------------|------------------------|
| | 12.5-13.0 | 13.0-13.5 | 13.5-14.0 |
| β | $0.39^{+0.06}_{-0.03}$ | $0.39^{+0.02}_{-0.02}$ | $0.38^{+0.01}_{-0.01}$ |
| $\log(S_{X,0})$ [$\text{erg s}^{-1} \text{kpc}^{-2}$] | $37.2^{+1.3}_{-0.3}$ | $37.3^{+0.1}_{-0.1}$ | $37.6^{+0.1}_{-0.1}$ |
| r_c [kpc] | 5^{+8}_{-4} | 10^{+3}_{-3} | 15^{+3}_{-3} |
| χ^2 | 4.5 | 4.4 | 16.0 |
| d.o.f. | 9 | 11 | 13 |
| $\chi^2/\text{d.o.f.}$ | 0.5 | 0.4 | 1.2 |

Notes. The uncertainty is of 1σ . We use the X-ray surface brightness profiles within R_{vir} for the fits.

where n_0 is the gas density at the galaxy center and is expressed as

$$n_0 = \sqrt{\frac{S_{X,0}\Gamma(3\beta)}{\sqrt{\pi}\epsilon_X \frac{n_e}{n_H} r_c \Gamma(3\beta - 1/2)}} \quad [\text{cm}^{-3}], \quad (5)$$

where n_e and n_H are the number densities of electrons and hydrogens, Γ is gamma function (Ge et al. 2016). We take the APEC model to estimate $\epsilon_X(T, Z)$, which is the normalized X-ray flux of thermal plasma with temperature T and metal abundance Z (Smith et al. 2001). We assume the temperature of the hot CGM is at the virial temperature T_{vir} , which can be derived from the M_{vir} and R_{vir} ¹⁶, or half virial temperature (to be conservative). The X-ray emissivity of the hot CGM at $T_{\text{vir}} < 1\text{keV}$ depends strongly on the metallicity abundance, which is not well studied for the MW-mass galaxies yet. We take values of $0.1Z_{\odot}$, $0.3Z_{\odot}$ and Z_{\odot} to estimate $\epsilon_X(T, Z)$. Z_{\odot} is detected at massive galaxy groups, and we take it as an upper limit (Gastaldello et al. 2021), $0.1Z_{\odot}$ is reported from the CGM of the Milky-Way (Ponti et al. 2023), and $0.3Z_{\odot}$ is a commonly used value for the hot CGM. We consider the uncertainties from temperature and metallicity abundance as systematic. The uncertainty of each assumption of temperature and metallicity abundance is estimated

¹⁶ For reference, the average M_{vir} of MW-mass, M31-mass, and 2M31-mass galaxies are taken as $1.3 \times 10^{12} M_{\odot}$, $4.2 \times 10^{12} M_{\odot}$, and $1.2 \times 10^{13} M_{\odot}$. The T_{vir} are taken as 0.22 keV, 0.5 keV, and 1.0 keV. The median M_{vir} of the three bins in $\log(M_{200m}) = 12.5 - 14.0$ of CEN_{halo} sample are $5.0 \times 10^{12} M_{\odot}$, $1.6 \times 10^{13} M_{\odot}$, and $4.3 \times 10^{13} M_{\odot}$. The T_{vir} are taken as 0.57 keV, 1.20 keV, and 2.65 keV.

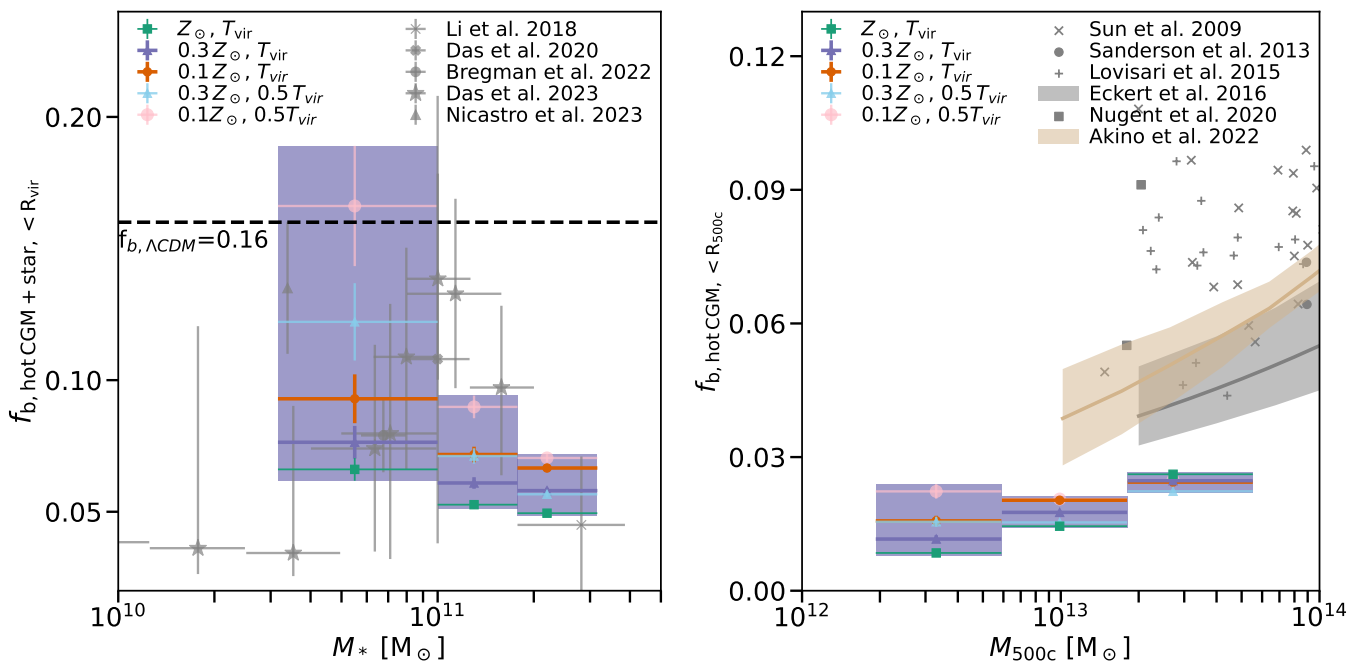


Fig. 7: Baryon fraction as a function of M_* given on the left. The baryon fraction is the sum of the stellar and the hot CGM within R_{vir} divided by the virial mass ($f_{b, \text{hot CGM} + \text{star}, < R_{\text{vir}}} = (M_{\text{hot CGM}, < R_{\text{vir}}} + M_*)/M_{\text{vir}}$). We assume that the metallicity abundance of the hot CGM is $0.1Z_{\odot}$, $0.3Z_{\odot}$ and Z_{\odot} , and the temperature of the hot CGM is at virial temperature (T_{vir}) or half ($0.5T_{\text{vir}}$). The baryon fractions predicted with different metallicity abundances and temperatures are summarised in purple square. The dashed line ($f_b = 0.16$) is the cosmological baryon fraction (Planck Collaboration et al. 2020). The gray points are taken from tSZ measurements (Bregman et al. 2022; Das et al. 2023), and X-ray measurements (Li et al. 2018; Das et al. 2020; Nicastro et al. 2023). Right panel shows the baryon fraction as a function of M_{500c} under assumptions of metallicity abundances and temperatures. The baryon fraction is the hot CGM within R_{500c} divided by the M_{500c} ($f_{b, \text{hot CGM}, < R_{500c}} = (M_{\text{hot CGM}, < R_{500c}})/M_{500c}$). The gray points are gas fractions estimated from detected clusters and groups in X-ray (Sun et al. 2009; Sanderson et al. 2013; Lovisari et al. 2015; Eckert et al. 2016; Nugent et al. 2020; Akino et al. 2022).

by propagating the 1σ uncertainty of β model considering the covariance of parameters therein.

We calculate the hot CGM mass ($M_{\text{CGM}, < R_{\text{vir}}}$) by integrating the density profile of the hot CGM within R_{vir} . For the CEN sample, we sum the hot CGM and stellar mass¹⁷ $M_b = M_{\text{CGM}, < R_{\text{vir}}} + M_*$, and calculate the baryon fraction by $f_{b, \text{hot CGM} + \text{star}, < R_{\text{vir}}} = M_b/M_{\text{vir}}$. The result of central galaxies with $\log(M_*) = 10.5 - 11.5$ is presented in the left panel of Fig. 7. For the MW-mass, M31-mass and 2M31-mass galaxies, we obtain $f_{b, \text{hot CGM} + \text{star}, < R_{\text{vir}}} = 0.12 \pm 0.06, 0.07 \pm 0.02, 0.06 \pm 0.01$, respectively. We compare our measurements to the f_b measured based on the X-ray and tSZ (Li et al. 2018; Das et al. 2020; Bregman et al. 2022; Das et al. 2023; Nicastro et al. 2023). We find consistent results of $f_{b, \text{hot CGM} + \text{star}, < R_{\text{vir}}}$ with literature within 1σ .

For the CEN_{halo} sample, we do not include the stellar component, and the baryon fraction within R_{vir} is defined by $f_{b, \text{hot CGM}, < R_{\text{vir}}} = M_{\text{CGM}, < R_{\text{vir}}}/M_{\text{vir}}$. For the galaxies with $M_{200m} = 12.5 - 13.0, 13.0 - 13.5$ and $13.5 - 14.0$, we obtain $f_{b, \text{hot CGM}, < R_{\text{vir}}} = 0.03 \pm 0.02, 0.04 \pm 0.01$ and 0.05 ± 0.005 for the three halo mass bins respectively. We compare our measurements to the $f_{b, \text{hot CGM}}$ measured within R_{500c} based on the X-ray emission and tSZ (Sun et al. 2009; Sanderson et al. 2013; Lovisari et al. 2015; Eckert et al. 2016; Nugent et al. 2020; Akino et al. 2022). To keep consistency, we also calculate the hot CGM fraction within R_{500c} ($f_{b, \text{hot CGM}, < R_{500c}} = M_{\text{CGM}, < R_{500c}}/M_{500c}$) by integrating the density

¹⁷ We do not include the satellite stellar mass when calculating the baryon fraction.

profile of the hot CGM within R_{500c} ¹⁸. The hot CGM fraction within R_{500c} is about 50% of the hot CGM fraction within R_{vir} . The result is presented in the right panel of Fig. 7. We find our $f_{b, \text{hot CGM}, < R_{500c}}$ is lower than the literature value, with the difference being approximately 2σ .

The ΛCDM cosmology theory predicts $f_b \approx 16\%$ (Planck Collaboration et al. 2020), as the dash line in Fig. 7. Our measured $f_{b, \text{hot CGM} + \text{star}}$ within the virial radius of galaxies are generally below the ΛCDM cosmology theory predicted. We obtain a hot CGM density profile with a slope $\approx r^{-1.2}$ within R_{vir} , which is flatter than the dark matter profile ($\approx r^{-3.0}$, NFW profile, Navarro et al. 1997). Consequently, as the integrated radius increases, the baryon fraction within that radius also increases. The relatively flat density profile of the hot CGM near the virial radius implies that hot baryons may extend beyond. If the hot CGM density profile can be extrapolated beyond the virial radius without a cutoff, the baryon fraction could reach the cosmological value within a few times R_{vir} .

Therefore, We extrapolate the baryon density profile measured within R_{vir} and the NFW profile to larger radii. We calculate the radius within which the baryon fraction exceeds 16% (namely the closure radius R_c defined in Ayromlou et al. (2023)¹⁹), the result is shown in Fig. 8. We take the baryon frac-

¹⁸ We convert the M_{200m} to M_{500c} with the mass-concentration relation model from Ishiyama et al. (2021) and calculate the R_{500c} .

¹⁹ Notice the R_c defined in Ayromlou et al. (2023) does not restrict to the central halo but considers all the dark matter and baryon within R_c . Differently, we restrict to the central halo by simple extrapolation of its

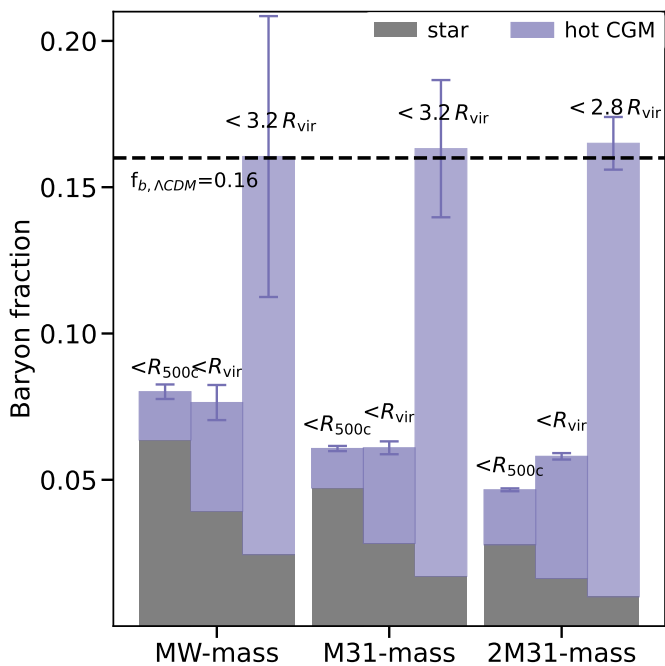


Fig. 8: Baryon fraction within R_{500c} , R_{vir} and the radius within which the baryon fraction exceeds 16% (R_c), for MW-mass, M31-mass and 2M31-mass galaxies. We take the baryon fraction derived from the assumption of T_{vir} and $0.3Z_{\odot}$. The error bar is the uncertainty propagated from the β model.

tion derived from the assumption of T_{vir} and $0.3Z_{\odot}$ to estimate R_c . We obtain closure radius $R_c \approx 3R_{vir}$ for MW-mass, M31-mass and 2M31-mass galaxies.

Future, more extensive galaxy surveys, such as DESI and 4MOST, will allow us to expand the galaxy sample and enhance the statistical power necessary to characterize the hot CGM profile beyond the virial radius accurately, therefore allowing us to either probe the presence of the baryons beyond the virial radius or determine the presence of a cut off in the hot CGM density distribution.

The low baryon fraction within R_{vir} might be due to the ejective feedback processes; for example, AGN outflows might push the baryons out of R_{vir} (Sorini et al. 2022; Ayromlou et al. 2023). The SIMBA simulation found $R_c \approx 15 R_{vir}$ for M31-mass galaxies and $R_c \approx 10 R_{vir}$ for 2M31-mass galaxies (Sorini et al. 2022). The IllustrisTNG simulation found $R_c \approx 5 R_{vir}$ and $R_c \approx 3 R_{vir}$, respectively (Ayromlou et al. 2023). The closure radii predicted in the simulations are generally larger than the $3 R_{vir}$ estimated from the observed and extrapolated hot CGM profile. The X-ray surface brightness profiles measured in this analysis provide a new benchmark for the simulations to implement the feedback processes therein.

Measuring the baryon mass through the X-ray emission method relies on the accurate assumption of the properties of the hot CGM. Our assumed temperatures and metallicity abundances may not be sufficient to cover the possible physical properties of the hot gas and introduce systematic errors. For example, the temperature of the hot CGM might decrease with radius. In such a case, our assumed isothermal profile overestimates the emissivity of the hot CGM. Besides, we do not consider the other

baryon and dark matter profiles, and do not consider the baryon and dark matter contribution from other halos.

phases of the CGM, namely, the less hot components that are not measured by the X-ray emission. Especially for the lower mass galaxies, the cool phase may occupy a higher share of the gas mass. For example, the SIMBA simulation predicts the gas with $T < 0.5T_{vir}$ contributes to about 2% baryon fraction for MW-mass galaxies (Sorini et al. 2022).

Our result only constitutes a first approximation and does not reflect the wealth of physical processes at stakes in the CGM (Faucher-Giguère & Oh 2023). We leave a detailed inference of the different baryonic components and their properties for future studies. With the progress of the metallicity abundance and temperature measurement, point source models, and better statistics from larger galaxy samples in the future, we can set better constraints on the CGM density profile of MW-mass and M31-mass galaxies. In particular, the X-ray microcalorimeter observations, with a high energy resolution, are expected to contribute significantly to this endeavor (Nandra et al. 2013; XRISM Science Team 2020; Cui et al. 2020).

8. Summary and conclusions

In this work, we provide a new detection of the X-ray emission from the hot circumgalactic medium (hot CGM) around large statistical samples of (massive) galaxies. We use the eRASS:4 X-ray data over an extra-galactic sky of about $11,000 \text{ deg}^2$. We achieved a significant step forward in understanding the influence and possible bias from the satellite galaxies (Figs. 1, 2 and 3). With the SDSS (spectroscopic) galaxy catalog and the group finder algorithm applied, we built two galaxy samples containing about 85,222 central galaxies split into stellar mass bins and 125,512 central galaxies split in halo mass bins (Table 3). We carefully model the components that can contaminate the CGM emission: the unresolved AGN and XRB in the stacked galaxies, the XRB in the satellite galaxies, and the satellite boost bias due to misclassified centrals (Sect. 4).

We stacked the galaxies, and the statistics we gained support the following main findings:

- We measured the mean X-ray surface brightness profiles for central galaxies with $\log(M_*) > 10.0$ or $\log(M_{200m}) > 11.5$ to unprecedentedly high S/N values (Fig. 4). We detected extended X-ray emission around $\log(M_*) > 10.5$ and $\log(M_{200m}) > 12.5$ galaxy populations out to R_{vir} . The S/Ns of the extended emission within R_{vir} are $> 3.1\sigma$ for $\log(M_*) > 10.5$ central galaxies and $> 2.8\sigma$ for central galaxies with $\log(M_{200m}) > 12.5$.
- For the first time, we have measured the mean X-ray surface brightness profile of hot CGM for approximately volume-limited central $\log(M_*) = 10.5 - 11.5$ or $\log(M_{200m}) = 12.5 - 14.0$ galaxy populations out to R_{vir} (Fig. 5 and Fig. 6). We fit a β model to the profiles and obtained $\beta \approx 0.4$ (Table 4). The measured X-ray surface brightness profiles are essential to constraining the galaxy evolution models in semi-analytic or hydrodynamic simulations.
- We conservatively assumed a range of temperatures and metallicity abundances of the hot CGM to infer its mass. The baryon fraction within R_{vir} is lower than the ΛCDM cosmology theory predicted and is consistent with literature measurements (Fig. 7). We extrapolate the measured hot CGM profile beyond R_{vir} and find within $\approx 3R_{vir}$ the baryon fraction is close to the ΛCDM cosmology theory (Fig. 8).

The eROSITA sky survey yields a vast repository of X-ray data across the sky, with abundant information on the hot CGM

that calls for further investigation and analysis. The measured X-ray surface brightness profiles of the FULL_{phot} have high S/N values, which allows for a complete model to be built, including the galaxy distribution and X-ray properties of the galaxy (Shreeram et al. in prep). With deeper galaxy surveys (e.g., 4MOST, DESI) we can enlarge the galaxy sample, increase the statistics, and obtain a better view of the hot CGM around dwarf galaxies ($\log(M_*) < 10$). With the continued progress of X-ray microcalorimeter observations, we will obtain a better knowledge of the metallicity and temperature of the CGM to derive its density profile.

Acknowledgements. We thank the anonymous referee for thoughtful comments that improved the manuscript. This project acknowledges financial support from the European Research Council (ERC) under the European Union's Horizon 2020 research and innovation program HotMilk (grant agreement No. 865637). GP acknowledges support from Bando per il Finanziamento della Ricerca Fondamentale 2022 dell'Istituto Nazionale di Astrofisica (INAF): GO Large program and from the Framework per l'Attrazione e il Rafforzamento delle Eccellenze (FARE) per la ricerca in Italia (R20L5S39T9). NT acknowledges support from NASA under award number 80GSFC21M0002. PP has received funding from the European Research Council (ERC) under the European Union's Horizon Europe research and innovation program ERC CoG (Grant agreement No. 101045437).

This work is based on data from eROSITA, the soft X-ray instrument aboard SRG, a joint Russian-German science mission supported by the Russian Space Agency (Roskosmos), in the interests of the Russian Academy of Sciences represented by its Space Research Institute (IKI), and the Deutsches Zentrum für Luft- und Raumfahrt (DLR). The SRG spacecraft was built by Lavochkin Association (NPOL) and its subcontractors, and is operated by NPOL with support from the Max Planck Institute for Extraterrestrial Physics (MPE).

The development and construction of the eROSITA X-ray instrument was led by MPE, with contributions from the Dr. Karl Remeis Observatory Bamberg & ECAP (FAU Erlangen-Nuernberg), the University of Hamburg Observatory, the Leibniz Institute for Astrophysics Potsdam (AIP), and the Institute for Astronomy and Astrophysics of the University of Tübingen, with the support of DLR and the Max Planck Society. The Argelander Institute for Astronomy of the University of Bonn and the Ludwig Maximilians Universität Munich also participated in the science preparation for eROSITA.

The eROSITA data shown here were processed using the eSASS/NRTA software system developed by the German eROSITA consortium.

Funding for the SDSS and SDSS-II has been provided by the Alfred P. Sloan Foundation, the Participating Institutions, the National Science Foundation, the U.S. Department of Energy, the National Aeronautics and Space Administration, the Japanese Monbukagakusho, the Max Planck Society, and the Higher Education Funding Council for England. The SDSS Web Site is <http://www.sdss.org/>. The SDSS is managed by the Astrophysical Research Consortium for the Participating Institutions. The Participating Institutions are the American Museum of Natural History, Astrophysical Institute Potsdam, University of Basel, University of Cambridge, Case Western Reserve University, University of Chicago, Drexel University, Fermilab, the Institute for Advanced Study, the Japan Participation Group, Johns Hopkins University, the Joint Institute for Nuclear Astrophysics, the Kavli Institute for Particle Astrophysics and Cosmology, the Korean Scientist Group, the Chinese Academy of Sciences (LAMOST), Los Alamos National Laboratory, the Max-Planck-Institute for Astronomy (MPIA), the Max-Planck-Institute for Astrophysics (MPA), New Mexico State University, Ohio State University, University of Pittsburgh, University of Portsmouth, Princeton University, the United States Naval Observatory, and the University of Washington.

The DESI Legacy Imaging Surveys consist of three individual and complementary projects: the Dark Energy Camera Legacy Survey (DECaLS), the Beijing-Arizona Sky Survey (BASS), and the Mayall z-band Legacy Survey (MzLS). DECaLS, BASS and MzLS together include data obtained, respectively, at the Blanco telescope, Cerro Tololo Inter-American Observatory, NSF's NOIRLab; the Bok telescope, Steward Observatory, University of Arizona; and the Mayall telescope, Kitt Peak National Observatory, NOIRLab. NOIRLab is operated by the Association of Universities for Research in Astronomy (AURA) under a cooperative agreement with the National Science Foundation. Pipeline processing and analyses of the data were supported by NOIRLab and the Lawrence Berkeley National Laboratory (LBNL). Legacy Surveys also uses data products from the Near-Earth Object Wide-field Infrared Survey Explorer (NEOWISE), a project of the Jet Propulsion Laboratory/California Institute of Technology, funded by the National Aeronautics and Space Administration. Legacy Surveys was supported by: the Director, Office of Science, Office of High Energy Physics of the U.S. Department of Energy; the National Energy Research Scientific Computing Center, a DOE Office of Science User Facility;

the U.S. National Science Foundation, Division of Astronomical Sciences; the National Astronomical Observatories of China, the Chinese Academy of Sciences and the Chinese National Natural Science Foundation. LBNL is managed by the Regents of the University of California under contract to the U.S. Department of Energy. The complete acknowledgments can be found at <https://www.legacysurvey.org/acknowledgment/>.

The Siena Galaxy Atlas was made possible by funding support from the U.S. Department of Energy, Office of Science, Office of High Energy Physics under Award Number DE-SC0020086 and from the National Science Foundation under grant AST-1616414.

References

- Abazajian, K. N., Adelman-McCarthy, J. K., Agüeros, M. A., et al. 2009, *ApJS*, 182, 543
- Abbott, T. M. C., Abdalla, F. B., Allam, S., et al. 2018, *ApJS*, 239, 18
- Abdullah, M. H., Wilson, G., & Klypin, A. 2018, *ApJ*, 861, 22
- Aiola, S., Calabrese, E., Maurin, L., et al. 2020, *J. Cosmology Astropart. Phys.*, 2020, 047
- Aird, J., Coil, A. L., & Georgakakis, A. 2017, *MNRAS*, 465, 3390
- Akino, D., Eckert, D., Okabe, N., et al. 2022, *PASJ*, 74, 175
- Almeida, A., Anderson, S. F., Argudo-Fernández, M., et al. 2023, *ApJS*, 267, 44
- Anderson, M. E., Churazov, E., & Bregman, J. N. 2016, *MNRAS*, 455, 227
- Anderson, M. E., Gaspari, M., White, S. D. M., Wang, W., & Dai, X. 2015, *MNRAS*, 449, 3806
- Andrae, R. 2010, arXiv e-prints, arXiv:1009.2755
- Arnouts, S., Cristiani, S., Moscardini, L., et al. 1999, *MNRAS*, 310, 540
- Ayromlou, M., Nelson, D., & Pillepich, A. 2023, *MNRAS*, 524, 5391
- Baldwin, J. A., Phillips, M. M., & Terlevich, R. 1981, *PASP*, 93, 5
- Beckwith, S. V. W., Stiavelli, M., Koekemoer, A. M., et al. 2006, *AJ*, 132, 1729
- Behroozi, P., Wechsler, R. H., Hearin, A. P., & Conroy, C. 2019, *MNRAS*, 488, 3143
- Bilicki, M., Dvornik, A., Hoekstra, H., et al. 2021, *A&A*, 653, A82
- Bilicki, M., Peacock, J. A., Jarrett, T. H., et al. 2016, *ApJS*, 225, 5
- Blanton, M. R., Schlegel, D. J., Strauss, M. A., et al. 2005, *AJ*, 129, 2562
- Bogdán, Á., Forman, W. R., Vogelsberger, M., et al. 2013, *ApJ*, 772, 97
- Bogdán, Á., Vogelsberger, M., Kraft, R. P., et al. 2015, *ApJ*, 804, 72
- Bregman, J. N., Hodges-Kluck, E., Qu, Z., et al. 2022, *ApJ*, 928, 14
- Brinchmann, J., Charlot, S., White, S. D. M., et al. 2004, *MNRAS*, 351, 1151
- Brunner, H., Liu, T., Lamer, G., et al. 2022, *A&A*, 661, A1
- Bruzual, G. & Charlot, S. 2003, *MNRAS*, 344, 1000
- Bryan, G. L. & Norman, M. L. 1998, *ApJ*, 495, 80
- Cavaliere, A. & Fusco-Femiano, R. 1976, *A&A*, 49, 137
- Chadayammuri, U., Bogdán, Á., Oppenheimer, B. D., et al. 2022, *ApJ*, 936, L15
- Chen, Y.-M., Kauffmann, G., Tremonti, C. A., et al. 2012, *MNRAS*, 421, 314
- Comparat, J., Luo, W., Merloni, A., et al. 2023, *A&A*, 673, A122
- Comparat, J., Merloni, A., Dwelly, T., et al. 2020, *A&A*, 636, A97
- Comparat, J., Merloni, A., Salvato, M., et al. 2019, *MNRAS*, 487, 2005
- Comparat, J., Truong, N., Merloni, A., et al. 2022, *A&A*, 666, A156
- Coupon, J., Arnouts, S., van Waerbeke, L., et al. 2015, *MNRAS*, 449, 1352
- Crook, A. C., Huchra, J. P., Martimbeau, N., et al. 2007, *ApJ*, 655, 790
- Cui, W., Chen, L. B., Gao, B., et al. 2020, *Journal of Low Temperature Physics*, 199, 502
- Dai, X., Anderson, M. E., Bregman, J. N., & Miller, J. M. 2012, *ApJ*, 755, 107
- Das, S., Chiang, Y.-K., & Mathur, S. 2023, *ApJ*, 951, 125
- Das, S., Mathur, S., & Gupta, A. 2020, *ApJ*, 897, 63
- de Jong, J. T. A., Verdoes Kleijn, G. A., Erben, T., et al. 2017, *A&A*, 604, A134
- de Jong, R. S., Agertz, O., Berbel, A. A., et al. 2019, *The Messenger*, 175, 3
- DESI Collaboration, Aghamousa, A., Aguilar, J., et al. 2016, arXiv e-prints, arXiv:1611.00036
- Dey, A., Schlegel, D. J., Lang, D., et al. 2019, *AJ*, 157, 168
- Driver, S. P., Bellstedt, S., Robotham, A. S. G., et al. 2022, *MNRAS*, 513, 439
- Eckert, D., Ettori, S., Coupon, J., et al. 2016, *A&A*, 592, A12
- Eckert, D., Gaspari, M., Gastaldello, F., Le Brun, A. M. C., & O'Sullivan, E. 2021, *Universe*, 7, 142
- Faucher-Giguère, C.-A. & Oh, S. P. 2023, *ARA&A*, 61, 131
- Finoguenov, A., Merloni, A., Comparat, J., et al. 2019, *The Messenger*, 175, 39
- Gastaldello, F., Simionescu, A., Mernier, F., et al. 2021, *Universe*, 7, 208
- Ge, C., Wang, Q. D., Tripp, T. M., et al. 2016, *MNRAS*, 459, 366
- HI4PI Collaboration, Ben Bekhti, N., Flöer, L., et al. 2016, *A&A*, 594, A116
- Hogg, D. W., Bovy, J., & Lang, D. 2010, arXiv e-prints, arXiv:1008.4686
- Hsu, L.-T., Salvato, M., Nandra, K., et al. 2014, *ApJ*, 796, 60
- Ilbert, O., Arnouts, S., McCracken, H. J., et al. 2006, *A&A*, 457, 841
- Ilbert, O., McCracken, H. J., Le Fèvre, O., et al. 2013, *A&A*, 556, A55
- Ishiyama, T., Prada, F., Klypin, A. A., et al. 2021, *MNRAS*, 506, 4210
- Ivezić, Ž., Kahn, S. M., Tyson, J. A., et al. 2019, *ApJ*, 873, 111

- Kereš, D., Katz, N., Davé, R., Fardal, M., & Weinberg, D. H. 2009a, *MNRAS*, 396, 2332
- Kereš, D., Katz, N., Fardal, M., Davé, R., & Weinberg, D. H. 2009b, *MNRAS*, 395, 160
- Kuijken, K., Heymans, C., Dvornik, A., et al. 2019, *A&A*, 625, A2
- Laigle, C., McCracken, H. J., Ilbert, O., et al. 2016, *ApJS*, 224, 24
- Laureijs, R., Amiaux, J., Arduini, S., et al. 2011, arXiv e-prints, arXiv:1110.3193
- Leauthaud, A., Tinker, J., Bundy, K., et al. 2012, *ApJ*, 744, 159
- Lehmer, B. D., Eufrasio, R. T., Tzanavaris, P., et al. 2019, *ApJS*, 243, 3
- Li, J.-T., Bregman, J. N., Wang, Q. D., Crain, R. A., & Anderson, M. E. 2016, *ApJ*, 830, 134
- Li, J.-T., Bregman, J. N., Wang, Q. D., Crain, R. A., & Anderson, M. E. 2018, *ApJ*, 855, L24
- Li, J.-T., Bregman, J. N., Wang, Q. D., et al. 2017, *ApJS*, 233, 20
- Li, J.-T. & Wang, Q. D. 2013, *MNRAS*, 428, 2085
- Linke, L., Simon, P., Schneider, P., et al. 2022, *A&A*, 665, A38
- Liu, A., Bulbul, E., Ghirardini, V., et al. 2022, *A&A*, 661, A2
- Locatelli, N., Ponti, G., Zheng, X., et al. 2024, *A&A*, 681, A78
- Lovisari, L., Reiprich, T. H., & Schellenberger, G. 2015, *A&A*, 573, A118
- McIntosh, A. 2016, arXiv e-prints, arXiv:1606.00497
- McMahon, R. G., Banerji, M., Gonzalez, E., et al. 2013, *The Messenger*, 154, 35
- Merloni, A., Lamer, G., Liu, T., et al. 2024, *A&A*, 682, A78
- Merloni, A., Predehl, P., Becker, W., et al. 2012, arXiv e-prints, arXiv:1209.3114
- Moster, B. P., Naab, T., & White, S. D. M. 2013, *MNRAS*, 428, 3121
- Moster, B. P., Naab, T., & White, S. D. M. 2020, *MNRAS*, 499, 4748
- Moster, B. P., Somerville, R. S., Maulbetsch, C., et al. 2010, *ApJ*, 710, 903
- Moustakas, J., Lang, D., Dey, A., et al. 2023, *ApJS*, 269, 3
- Naab, T. & Ostriker, J. P. 2017, *ARA&A*, 55, 59
- Nandra, K., Barret, D., Barcons, X., et al. 2013, arXiv e-prints, arXiv:1306.2307
- Navarro, J. F., Frenk, C. S., & White, S. D. M. 1997, *ApJ*, 490, 493
- Nicastro, F., Krongold, Y., Fang, T., et al. 2023, *ApJ*, 955, L21
- Nugent, J. M., Dai, X., & Sun, M. 2020, *ApJ*, 899, 160
- Onken, C. A., Wolf, C., Bessell, M. S., et al. 2019, *PASA*, 36, e033
- Oppenheimer, B. D., Babul, A., Bahé, Y., Butsky, I. S., & McCarthy, I. G. 2021, *Universe*, 7, 209
- Planck Collaboration, Abergel, A., Ade, P. A. R., et al. 2014, *A&A*, 571, A11
- Planck Collaboration, Aghanim, N., Akrami, Y., et al. 2020, *A&A*, 641, A6
- Ponti, G., Zheng, X., Locatelli, N., et al. 2023, *A&A*, 674, A195
- Pratt, G. W., Arnaud, M., Biviano, A., et al. 2019, *Space Sci. Rev.*, 215, 25
- Predehl, P., Andritschke, R., Arefiev, V., et al. 2021, *A&A*, 647, A1
- Prochaska, J. X., Weiner, B., Chen, H. W., Mulchaey, J., & Cooksey, K. 2011, *ApJ*, 740, 91
- Prochaska, J. X., Werk, J. K., Worseck, G., et al. 2017, *ApJ*, 837, 169
- Putman, M. E., Peek, J. E. G., & Joung, M. R. 2012, *ARA&A*, 50, 491
- Robotham, A. S. G., Norberg, P., Driver, S. P., et al. 2011, *MNRAS*, 416, 2640
- Sanderson, A. J. R., O'Sullivan, E., Ponman, T. J., et al. 2013, *MNRAS*, 429, 3288
- Shen, S., Mo, H. J., White, S. D. M., et al. 2003, *MNRAS*, 343, 978
- Skrutskie, M. F., Cutri, R. M., Stiening, R., et al. 2006, *AJ*, 131, 1163
- Smith, R. K., Brickhouse, N. S., Liedahl, D. A., & Raymond, J. C. 2001, *ApJ*, 556, L91
- Sorini, D., Davé, R., Cui, W., & Appleby, S. 2022, *MNRAS*, 516, 883
- Strauss, M. A., Weinberg, D. H., Lupton, R. H., et al. 2002, *AJ*, 124, 1810
- Strickland, D. K., Heckman, T. M., Colbert, E. J. M., Hoopes, C. G., & Weaver, K. A. 2004, *ApJS*, 151, 193
- Sun, M., Voit, G. M., Donahue, M., et al. 2009, *ApJ*, 693, 1142
- Sunyaev, R., Arefiev, V., Babushkin, V., et al. 2021, *A&A*, 656, A132
- Tempel, E., Kipper, R., Tamm, A., et al. 2016, *A&A*, 588, A14
- Tempel, E., Kruuse, M., Kipper, R., et al. 2018, *A&A*, 618, A81
- Tinker, J. L. 2021, *ApJ*, 923, 154
- Tinker, J. L. 2022, *AJ*, 163, 126
- Truong, N., Pillepich, A., & Werner, N. 2021, *MNRAS*, 501, 2210
- Truong, N., Pillepich, A., Werner, N., et al. 2020, *MNRAS*, 494, 549
- Tüllmann, R., Pietsch, W., Rossa, J., Breitschwerdt, D., & Dettmar, R. J. 2006, *A&A*, 448, 43
- Tumlinson, J., Peebles, M. S., & Werk, J. K. 2017, *ARA&A*, 55, 389
- Tumlinson, J., Thom, C., Werk, J. K., et al. 2011, *Science*, 334, 948
- van de Voort, F., Quataert, E., Hopkins, P. F., et al. 2016, *MNRAS*, 463, 4533
- Walker, S., Simionescu, A., Nagai, D., et al. 2019, *Space Sci. Rev.*, 215, 7
- Wang, Q. D. 2010, *Proceedings of the National Academy of Science*, 107, 7168
- Wechsler, R. H. & Tinker, J. L. 2018, *ARA&A*, 56, 435
- Werk, J. K., Prochaska, J. X., Cantalupo, S., et al. 2016, *ApJ*, 833, 54
- Werk, J. K., Prochaska, J. X., Tumlinson, J., et al. 2014, *ApJ*, 792, 8
- Wilms, J., Allen, A., & McCray, R. 2000, *ApJ*, 542, 914
- Wright, E. L., Eisenhardt, P. R. M., Mainzer, A. K., et al. 2010, *AJ*, 140, 1868
- XRISM Science Team. 2020, arXiv e-prints, arXiv:2003.04962
- Yang, X., Mo, H. J., van den Bosch, F. C., & Jing, Y. P. 2005, *MNRAS*, 356, 1293
- Yao, Y., Wang, Q. D., Hagihara, T., et al. 2009, *ApJ*, 690, 143
- Zehavi, I., Zheng, Z., Weinberg, D. H., et al. 2011, *ApJ*, 736, 59
- Zhang, Y., Comparat, J., Ponti, G., et al. 2024, arXiv e-prints, arXiv:2401.17309
- Zou, H., Gao, J., Zhou, X., & Kong, X. 2019, *ApJS*, 242, 8
- Zou, H., Sui, J., Xue, S., et al. 2022, *Research in Astronomy and Astrophysics*, 22, 065001
- Zu, Y. & Mandelbaum, R. 2016, *MNRAS*, 457, 4360

Appendix A: Validation of the background calculation

We test different methods to estimate the average background for the stacked galaxies.

Method a) We retrieve events within 3 Mpc of a random point which is located within the $1 - 4 \times R_{\text{vir}}$ of the galaxy (CUBE_{rd}). We merge CUBE_{rd} of each galaxy sample and calculate the mean $S_{X,\text{rd}}$ within 3 Mpc. As CUBE_{rd} is randomly distributed over the sky area of stacked galaxies, $S_{X,\text{rd}}$ is the average X-ray background of the stacked area.

Method b) We estimate the background surface brightness ($S_{X,\text{Mpc}}$) by taking the mean $S_{X,\text{gal}}$ within the annulus at 2-3 Mpc distance from the center. The annulus choice of the $S_{X,\text{Mpc}}$ guarantees that it is well beyond the virial radius of the largest haloes, namely the galaxy clusters. Method c) We define $S_{X,\text{min}}$ as the minimum value of $S_{X,\text{gal}}$ between R_{500c} and $2 \times R_{\text{vir}}$.

The X-ray surface brightness profiles of MW-mass galaxies in the FULL_{phot}, isolated and CEN samples compared to the different background estimates are presented in Fig. A.1. Beyond about 2 Mpc, the X-ray surface brightness profiles converge to $S_{X,\text{rd}}$ (method a), meaning the average background is properly recovered by the methods. For the FULL_{phot} sample, the difference between the three background estimates is less than 0.3% (at all radii), which is less than the uncertainty of each background. Therefore, the method used to estimate the background does not influence the result, and we take $S_{X,\text{min}}$ as the background estimation for FULL_{phot} (or FULL_{spec}).

The environment in which galaxies live may cause the local X-ray background to differ from the average background. In particular, the X-ray background towards isolated galaxies is expected (and observed) to be lower than the average, as they are selected in projection to live in sparse environments and have fewer foreground and background galaxies contributing to the X-ray background along that line of sight. Central galaxies, defined as the most massive galaxies in their local environment (virial halo), are expected to have only lower-mass foreground and background galaxies within their virial halo projection. Therefore, along the line of sight towards central galaxies, the local X-ray background is also lower than average but this effect is less severe than for isolated galaxies.

For the isolated sample, the observed X-ray surface brightness decreases up to R_{vir} and then increases until reaching the $S_{X,\text{rd}}$ at 2Mpc, as we discussed above (also see isolated galaxy definition in Appendix D). The difference between $S_{X,\text{min}}$ and $S_{X,\text{rd}}$ is about $4.1\% S_{X,\text{rd}}$. We take $S_{X,\text{min}}$ as the proper local background estimate for the isolated galaxy sample. The X-ray surface brightness of the CEN sample decreases until $1 - 2 R_{\text{vir}}$, then increases to the $S_{X,\text{rd}}$ (agrees within 1σ) but to a lesser extent than the isolated sample. The difference between the three background estimates is about $1.5\% S_{X,\text{rd}}$. We also take $S_{X,\text{min}}$ as the proper local background of the central galaxy samples (CEN and CEN_{halo}). We use the satellite galaxy samples (SAT and SAT_{halo}) to model the contamination from the misclassified centrals in the CEN and CEN_{halo} samples. To keep consistency, we also take $S_{X,\text{min}}$ as the background for SAT and SAT_{halo}. In summary, we take the $S_{X,\text{min}}$ as the proper background in all of our samples.

The background surface brightness is redshift-dependent in units of $\text{erg s}^{-1} \text{kpc}^{-2}$. The $S_{X,\text{rd}}$ background levels of the isolated and CEN samples are therefore different by a factor of about $(\frac{1+z_{\text{iso}}}{1+z_{\text{cen}}})^5$, where z_{iso} and z_{cen} are the median redshifts of the isolated and ‘CEN’ sample.

Appendix B: Merge SGA catalog to LS DR9 catalog

The SGA is a multi-wavelength atlas of nearby galaxies selected from DESI Legacy Imaging Surveys DR9. The selection is based on the apparent angular diameter of galaxies that are large enough to be spatially resolved. In the western Galactic hemisphere, there are 194527 galaxies in the SGA catalog. We match SGA to the LS DR9 catalog and find about 15% galaxies in SGA have no match in LS DR9. We add the missing SGA galaxies to the LS DR9 catalog to avoid losing the nearby massive galaxies.

No M_* information is provided in SGA, and about 34% of SGA galaxies have no redshift estimation. For SGA galaxies with a redshift estimate, we estimate the stellar mass by the SED fitting using the three optical bands (g,r,z) and two infrared bands (W1, W2), following the method in Zou et al. (2019). The galaxies without redshift estimation are thrown away due to the difficulty of estimating stellar mass. There are about 5% galaxies that fall in the stacking area with no photometry information and low-quality redshift and M_* , which we throw away. We match the remaining SGA galaxies to GAMA and find that our derived redshift and M_* are good quality. We add the 15,735 missing SGA galaxies with $\log(M_*) > 9$ to the LS DR9 catalog. 90% of these galaxies have $z < 0.1$.

Besides, galaxies in the LS DR9 catalog could be too close to the bright nearby SGA galaxy. This may affect the accuracy of z_{phot} or M_* in the LS DR9 catalog. We mask the LS DR9 galaxies that are within the R_{25} of SGA galaxies, where R_{25} is the approximate major-axis radius at the 25 mag arcsec⁻², which can be taken as the radius of galaxy disk. Notice that we did not consider the inclination and position angle of the SGA galaxy. The procedure above removes 0.01% of LS DR9 galaxies.

Appendix C: AGN model for CEN sample

Table C.1: Percentage and number of galaxy hosting AGN in CEN and CEN_{halo} sample, identified using the BPT diagram (Baldwin et al. 1981; Brinchmann et al. 2004).

| $\log(M_*)$ | f_{AGN} | N_{CENAGN} |
|------------------|------------------|---------------------|
| 10.0-10.5 | 16% | 1261 |
| 10.5-11.0 | 18% | 5421 |
| 11.0-11.25 | 14% | 3447 |
| 11.25-11.5 | 8% | 1505 |
| $\log(M_{200m})$ | f_{AGN} | N_{CENAGN} |
| 11.5-12.0 | 9% | 2396 |
| 12.0-12.5 | 17% | 7113 |
| 12.5-13.0 | 13% | 3965 |
| 13.0-13.5 | 4% | 849 |
| 13.5-14.0 | 2% | 170 |

We estimate the AGN contamination in the CEN sample based on observations. We select the central galaxies hosting AGN, identified as AGN or composite, based on the BPT diagram, and name it as CEN_{AGN} (Baldwin et al. 1981; Brinchmann et al. 2004). The percentage of central galaxies identified as hosting AGN (f_{AGN}) is listed in Table C.1. We stack the CEN_{AGN} sample in the same bins as the CEN sample, and mask detected X-ray sources. The obtained X-ray surface brightness profile for the MW-mass CEN_{AGN} galaxies is plotted in the left panel of Fig. C.1. The maximal X-ray emission originating from the unresolved point sources (AGN and XRB) in the stacked galax-

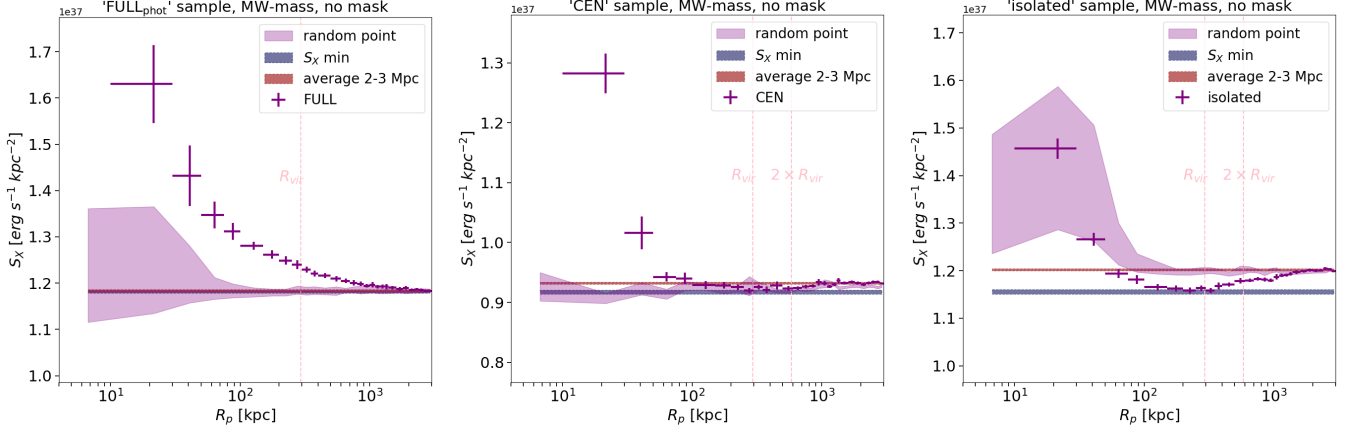


Fig. A.1: Observed X-ray surface brightness profiles of $\text{FULL}_{\text{phot}}$ sample (left), CEN sample (middle) and isolated sample (right), without masking X-ray sources. The data points are the observed X-ray surface brightness profile, the colored bands are the estimated background by taking the random points (purple), the minimum X-ray surface brightness (blue) and the mean X-ray surface brightness within 2-3 Mpc (red).

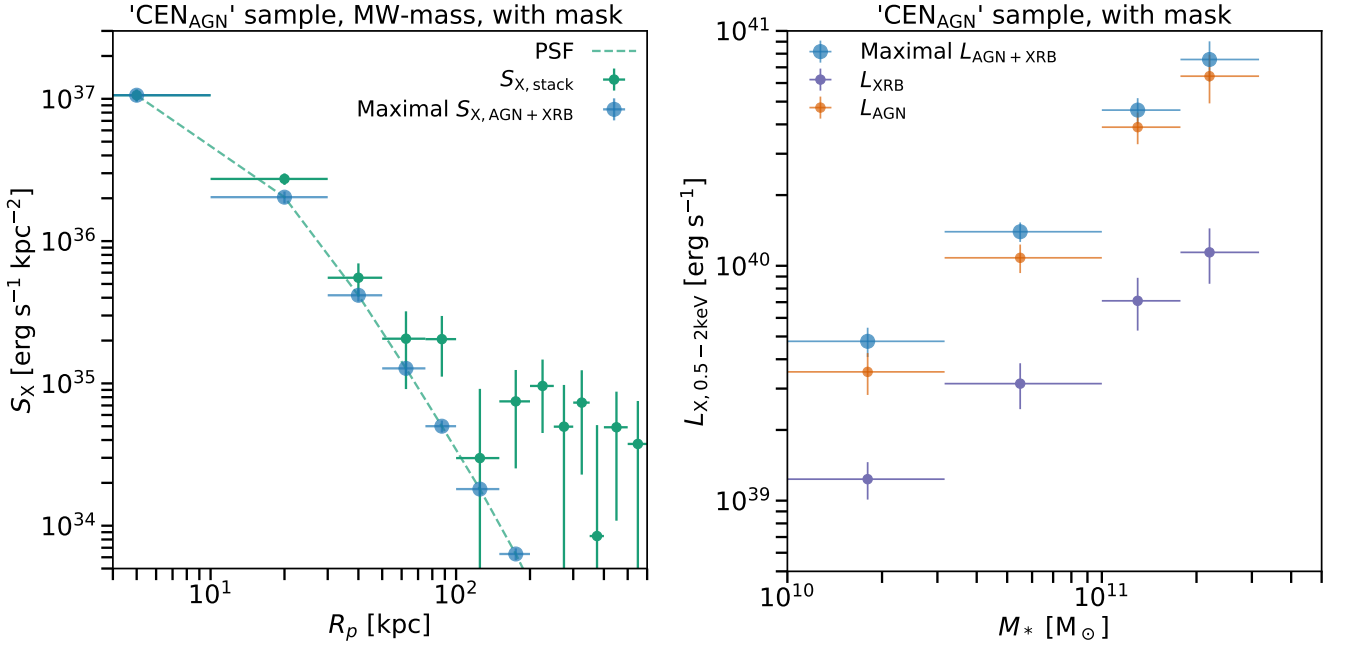


Fig. C.1: X-ray surface brightness profile of MW-mass galaxies (left) in CEN_{AGN} sample, after subtracting background and masking X-ray sources (green points), the maximal X-ray emission from the unresolved point sources (blue points), in the shape of PSF (green dashed line). Observed maximal X-ray luminosity (right) of unresolved point source (blue), the model predicted XRB luminosity (purple), and the residual X-ray luminosity of unresolved AGN (orange).

ies should be in the shape of PSF, with the first bin as bright as detected (green dots). The maximal X-ray luminosity of the unresolved point sources is calculated by integrating the X-ray emission in the shape of PSF out to R_{500c} . We subtract the XRB luminosity predicted by the empirical model (L_{XRB}) (Aird et al. 2017), and obtain the maximal unresolved AGN emission in the stacked galaxies (L_{AGN} , see right panel of Fig. C.1). For the galaxies identified as hosting AGN, the unresolved AGN X-ray emission is about 3 – 5 times brighter than the XRB. We notice that only $< 20\%$ galaxies in the CEN or CEN_{halo} samples are identified as hosting AGNs; we summarize that after averaging, the unresolved AGN emission is comparable or subdominant compared to the XRBs for the CEN or CEN_{halo} samples.

Appendix D: Isolated galaxy sample and stacking

Appendix D.1: Build isolated galaxy sample from LS DR9

Unlike spectroscopic surveys such as SDSS, the central galaxy selection algorithm by group finder is not readily applicable to LS DR9 due to its photometric redshift uncertainties. Instead, we construct an ‘isolated’ galaxy sample from LS DR9 that is, as much as possible, free from satellite contamination.

We work with projected haloes, as we illustrate schematically in Fig. D.1. For each galaxy, based on its stellar mass, we compute its mean virial radius (R_{vir}) and the angle it subtends on the sky (θ_{vir}) using the stellar to halo mass relation from Moster et al. (2010). The virial radius definition is that of Bryan & Nor-

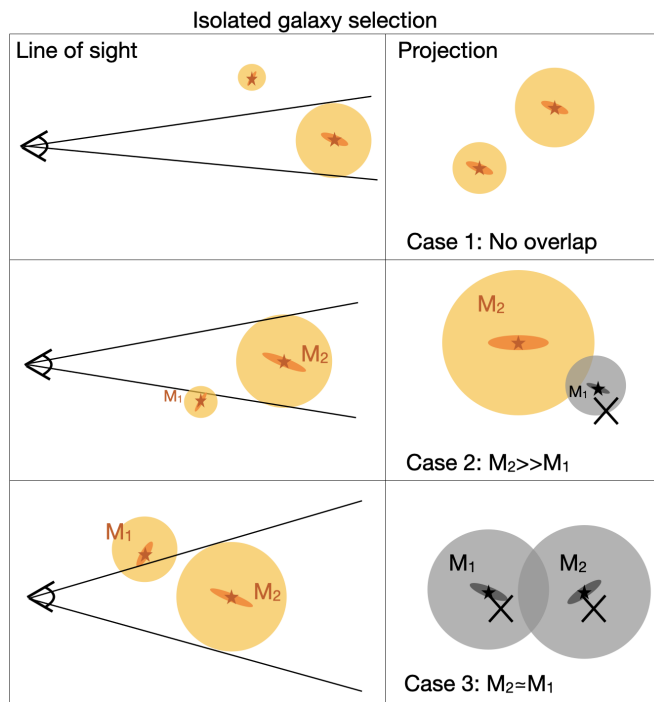


Fig. D.1: Illustration of how the isolated selection works for photometric samples. If after projection, the virial halo of a galaxy has no overlap or is much more massive than overlapped galaxies, they are kept in the isolated galaxy sample (in orange color). Otherwise, they are removed (in color gray). The radius of the largest circle denotes the virial radius of the galaxy (not to scale).

man (1998). In the simplest case (case 1), if the virial halo of a galaxy has no overlap with other galaxy halos along the line of sight (i.e., the angular separation of a galaxy pair is larger than the sum of their virial radii), then we assume it is naturally central and does not suffer from satellite contamination. In the case where the virial halo of a galaxy overlaps with other galaxy halos along the line of the sight (case 2, case 3), we select the galaxy that is dominantly more massive (by a factor of two) and remove the smaller galaxy from the sample (case 2). If the two galaxies have comparable stellar masses (the stellar mass difference is smaller than two), we reject both galaxies. In this way, we get the central galaxy at least twice as massive as the most massive satellite galaxy in its halo. It means that the satellite boost and the contamination from the sources in satellite galaxies are reduced. The sample is a (incomplete) sub-sample of the central galaxy population living in under-dense environments. The X-ray background for the isolated galaxies is lower than the average X-ray background over the sky (due to the selection method of isolated galaxies), and this necessitates taking $S_{X,\min}$ as the background (see the discussion in Appendix A). The selection of isolated galaxies has a low dependence on the photometric redshift accuracy of the galaxies.

The selection method used to construct the isolated galaxy sample is validated through the mock galaxy catalog. We build a mock LS DR9 catalog from the light cone we build in Sect. 4.1 up to $z=0.45$. We apply the magnitude cut $r_{AB} < 21$ to the light cone. We add a Gaussian distributed z_{error} and M_{error} with the same median and dispersion of the LS DR9 catalog to the corresponding accurate values provided by the light cone. Then we select the galaxies within the same M_* and z_{phot} bins as FULL_{phot} to build the mock FULL_{phot} sample. We apply the isolated galaxy

selection scheme to the mock FULL_{phot} sample and obtain a mock isolated sample. We use the mock samples to assess the isolated selection effect of our galaxy samples. In the mock FULL_{phot} sample, we find that the satellite fraction amounts to 25-35%. In the mock isolated sample, we get much lower satellite fractions, only 5-10%. In most cases, the satellite galaxies are kept since they are far away from other massive galaxies. A small portion of the satellite galaxies are misidentified due to the dispersion of z_{phot} and M_* of LS DR9. We also use the mock LS DR9 catalog to derive the stacked galaxies' average underlying M_{halo} and R_{vir} .

Isolated galaxy sample (isolated)

Following the scheme defined above, we select the isolated galaxies from the FULL_{phot} sample to minimize the projected X-ray emission from nearby galaxies. Considering the dispersion of the z_{phot} and M_* of LS DR9, we increase the 'FULL_{phot}' galaxy sample by retrieving galaxies with $z_{\text{phot}} < z_{\text{max}} + 0.05$ and $M_* > 1/2M_{\text{min}}$ to avoid extra selection of isolated galaxy.

The fraction of isolated galaxies selected from the FULL_{phot} sample is 25% at the lower mass end, 17% for MW-mass bin, 8% for M31-mass bin, and 5% for 2M31-mass bin. Table 3 details the total number of isolated galaxies obtained for each sample. We name the isolated galaxy sample as 'isolated'. In total, we have 213,514 isolated galaxies, about 2.5 times the CEN sample size, about 13 times larger than Comparat et al. (2022), 130 times larger than Chadayammuri et al. (2022) and close to the sample size of Anderson et al. (2015).

Two main differences exist between this isolated sample and the CEN sample. First, the isolated galaxies are central galaxies with at most $M_{\text{sat}} = 1/2M_{\text{cen}}$ satellites in the halo, and the satellite boost is well removed. Therefore, the isolated galaxies are located in a less dense environment than the CEN sample and should be considered as a subsample of the central galaxy population. Second, the redshift distributions of the isolated and CEN samples are different, with the isolated sample extending to $z = 0.4$.

Appendix D.2: The X-ray surface brightness profiles of isolated sample

The X-ray surface brightness profiles up to R_{vir} of the isolated sample in MW-mass, M31-mass and 2M31-mass are plotted in Fig. D.2. The X-ray emission detected here is the sum of unresolved point sources and hot gas emission. The X-ray surface brightness increases with stellar mass. Extended X-ray emission is detected beyond about 50 kpc for MW-mass and more massive galaxies. The profile becomes more extended with increasing stellar mass. The X-ray emission is detected within the virial radius of galaxies with $S/N \approx 3.0, 4.9, 3.7$ for the MW-mass, M31-mass, and 2M31-mass galaxies in the isolated sample.

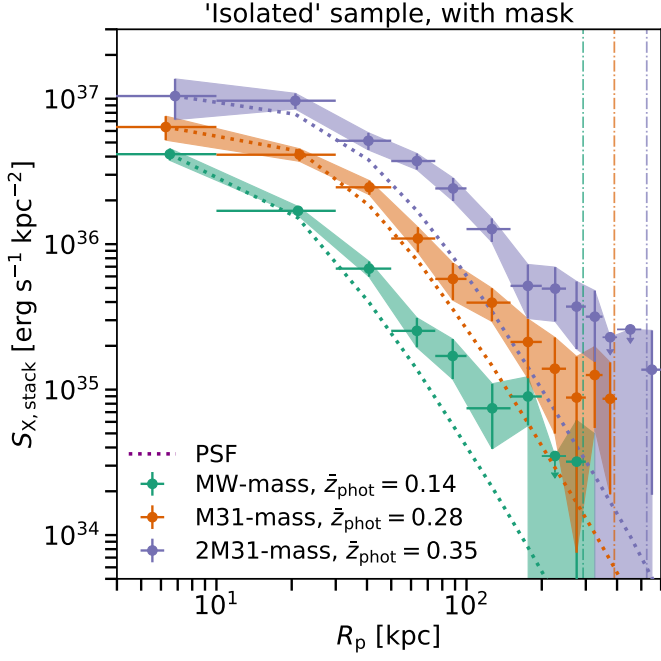


Fig. D.2: Mean X-ray surface brightness profiles of the isolated sample (with a magnitude limit of $r_{\text{AB}} < 20$) after subtracting background and masking X-ray sources, for galaxies with $\log(M_*) = 10.5 - 11.0$ (MW-mass), $11.0-11.25$ (M31-mass) and $11.25-11.5$ (2M31-mass). The X-ray emission comprises unresolved point sources and hot gas. \bar{z} is the median redshift of galaxies in each mass bin. The dotted lines are the PSF of eROSITA. The vertical dash-dotted lines are the virial radius at different stellar mass bins correspondingly.